

AD _____

Award Number: W81XWH-06-1-0003

TITLE: Intra-Operative Dosimetry in Prostate Brachytherapy

PRINCIPAL INVESTIGATOR: Ameet Jain

CONTRACTING ORGANIZATION: Johns Hopkins University
Baltimore, MD 21218-2686

REPORT DATE: April 2008

TYPE OF REPORT: Annual Summary Addendum

PREPARED FOR: U.S. Army Medical Research and Materiel Command
Fort Detrick, Maryland 21702-5012

DISTRIBUTION STATEMENT: Approved for Public Release;
Distribution Unlimited

The views, opinions and/or findings contained in this report are those of the author(s) and should not be construed as an official Department of the Army position, policy or decision unless so designated by other documentation.

REPORT DOCUMENTATION PAGE				Form Approved OMB No. 0704-0188	
Public reporting burden for this collection of information is estimated to average 1 hour per response, including the time for reviewing instructions, searching existing data sources, gathering and maintaining the data needed, and completing and reviewing this collection of information. Send comments regarding this burden estimate or any other aspect of this collection of information, including suggestions for reducing this burden to Department of Defense, Washington Headquarters Services, Directorate for Information Operations and Reports (0704-0188), 1215 Jefferson Davis Highway, Suite 1204, Arlington, VA 22202-4302. Respondents should be aware that notwithstanding any other provision of law, no person shall be subject to any penalty for failing to comply with a collection of information if it does not display a currently valid OMB control number. PLEASE DO NOT RETURN YOUR FORM TO THE ABOVE ADDRESS.					
1. REPORT DATE 01-04-2008		2. REPORT TYPE Annual Summary Addendum		3. DATES COVERED 14 Oct 2007– 14 Mar 2008	
4. TITLE AND SUBTITLE Intra-Operative Dosimetry in Prostate Brachytherapy				5a. CONTRACT NUMBER	
				5b. GRANT NUMBER W81XWH-06-1-0003	
				5c. PROGRAM ELEMENT NUMBER	
6. AUTHOR(S) Ameet Jain Email: jain@cs.jhu.edu				5d. PROJECT NUMBER	
				5e. TASK NUMBER	
				5f. WORK UNIT NUMBER	
7. PERFORMING ORGANIZATION NAME(S) AND ADDRESS(ES) Johns Hopkins University Baltimore, MD 21218-2686				8. PERFORMING ORGANIZATION REPORT NUMBER	
9. SPONSORING / MONITORING AGENCY NAME(S) AND ADDRESS(ES) U.S. Army Medical Research and Materiel Command Fort Detrick, Maryland 21702-5012				10. SPONSOR/MONITOR'S ACRONYM(S)	
				11. SPONSOR/MONITOR'S REPORT NUMBER(S)	
12. DISTRIBUTION / AVAILABILITY STATEMENT Approved for Public Release; Distribution Unlimited					
13. SUPPLEMENTARY NOTES					
14. ABSTRACT Favorable outcome in prostate brachytherapy critically depends on the accurate placement of radioactive sources in their planned locations. Unfortunately, there is variety of mechanical factors that cause the seeds to divert from their planned locations. While this problem has been known to brachytherapists, current technology does not allow for reliable localization of the implanted sources, thereby prohibiting the prediction and modification of seed distribution intra-operatively. The Research Objective of the proposal is to develop and evaluate ex-vivo a method for intra-operative localization of the implanted seeds in relation to the prostate, to facilitate in-situ dosimetric optimization and exit dosimetry. In particular, we will: [1] Registration of Ultrasound to Fluoroscopy (RUF): Develop methods for reconstruction of seed implants from X-ray fluoroscopy and spatially register them to the prostate anatomy identified in TRUS [2] System Integration: Integrate the above methods in a software package and link it with the FDA-approved CMS Interplant® prostate brachytherapy system to enable in-situ dosimetry calculation [3] Experimental Validation: Evaluate the performance of the RUF system on phantoms and pre-recorded patient data.					
15. SUBJECT TERMS Prostate Brachytherapy, X-ray reconstruction, C-arm, TRUS					
16. SECURITY CLASSIFICATION OF:			17. LIMITATION OF ABSTRACT	18. NUMBER OF PAGES	19a. NAME OF RESPONSIBLE PERSON
a. REPORT	b. ABSTRACT	c. THIS PAGE			USAMRMC
U	U	U	UU	31	19b. TELEPHONE NUMBER (include area code)

Table of Contents

Introduction.....	4
Body.....	4
Key Research Accomplishments.....	5
Reportable Outcomes.....	5
Conclusions.....	5
References.....	6
Appendices.....	7

A INTRODUCTION

For several decades, the definitive treatment for low and medium risk prostate cancer was radical prostatectomy or external beam radiation therapy, but low dose rate permanent seed brachytherapy (shortly brachytherapy) today can achieve equivalent outcomes. Brachytherapy, if accurately executed, can achieve a sharp demarcation between the treated volume and healthy structures, and thereby achieve superior tumor control with reduced morbidity. In contemporary practice, however, faulty needle and source placement often cause insufficient dose to the cancer and/or inadvertent radiation of the rectum, urethra, and bladder. Another fallacy of the current implant techniques is that reliable and accurate exit dosimetry is not possible. The contribution of the proposed research will be making C-arm fluoroscopy available for safe, simple, and robust intra-operative localization of brachytherapy sources relative to the prostate. We will develop a method for the registration of ultrasound to fluoroscopy (RUF), to fuse TRUS (Trans-rectal ultrasound can view the prostate but not the seeds) with C-arm fluoroscopy (which is capable of viewing the seeds but not the prostate). This feature will allow for dosimetric optimization of the prostate brachytherapy implants and exit dosimetry before the patient is released from the operating room; thereby enabling significant improvement on current clinical practice. A further promise is that fluoroscopy-based exit dosimetry may obviate CT-based post-implant dosimetry.

B BODY

B.1 Brief System Concept

The system concept for registration of ultrasound to fluoroscopy (RUF) is summarized in Figure 1. The fluoroscope is calibrated and corrected from image distortion pre-operatively. The implant procedure starts as usual: TRUS is used to guide each individual needle and a C-arm placed over the patient's abdomen. The C-arm is tracked with an X-ray fiducial system called FTRAC that is composed of optimally selected polynomial space curves. The fiducials are mounted rigidly to the TRUS frame in the field of view in a known calibrated pose relative to the TRUS, thereby providing spatial registration between the C-arm and TRUS. Upon implanting a batch of needles (typically a row of needles), we collect a set of TRUS

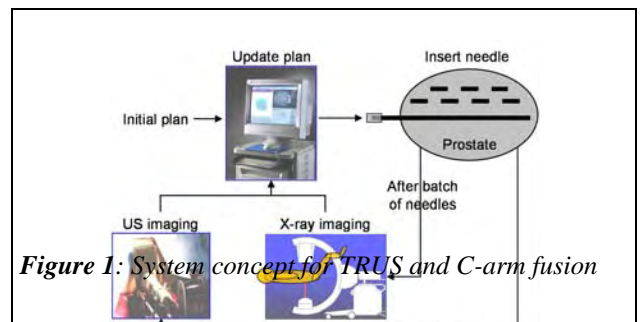


Figure 1: System concept for TRUS and C-arm fusion

and C-arm images. The locations of the implanted seeds are recovered from the C-arm fluoroscopy images with the use of a network flow based method called MARSHAL that provides seed segmentation, matching, and reconstruction method. Then the cloud of seeds is superimposed over the spatially co-registered TRUS images. The 3D dose distribution is rapidly calculated from the union of the already and yet to be implanted seeds. The dose distribution is analyzed with tools currently available in the brachytherapy system used. Then the implant plan can be optimized to account for discrepancies from the ideal dose distribution. The procedure continues with the next batch of needles in the cycle described above. After the last needle, a complete dosimetry check is performed, which provides a final opportunity to patch up any cold spots with additional seeds.

B.2 Proposed Statement of Work

We proposed to develop a method for the registration of ultrasound to fluoroscopy (RUF) to allow for intra-operative dosimetry in prostate brachytherapy and prototype mathematical algorithms (Aim-1), integrate them with an existing FDA approved prostate brachytherapy system that provides dosimetry analysis (Aim-2), and evaluate the system experimentally on phantoms and pre-recorded patient data (Aim-3). Algorithmic design (Aim-1) and experimental evaluation (Aim-3), will progress hand in hand. System integration (Aim-2) will be

performed immediately when a workable subset of RUF package becomes available from Aim-1 and again revisited towards at the end of the project. Therefore, the timeline will be somewhat non-linear. The detailed statement of work was as follows:

- Aim-1: Registration of Ultrasound to Fluoroscopy (RUF):** Develop a methods for reconstruction of seed implants from X-ray fluoroscopy and spatially registering them to the prostate anatomy identified in TRUS
- Aim-2: System Integration:** Integrate the above methods in a software package and link it with the FDA-approved CMS Interplant® prostate brachytherapy system to enable dosimetry calculation
- Aim-3: Experimental Validation:** Evaluate the performance of the RUF system on phantoms and pre-recorded patient data. (Neither of which require an IRB approval)

B.3 Progress Report for Second Year

In the previous report in Nov 2007, we accomplished all the proposed project aims. We made further progress, in addition to what was promised, and delivered a system that worked intra-operatively during the surgery (vs a system that will successfully be validated on pre-recorded data).

This extension was taken, predominantly to document all the work into publications and present them. The goal was successfully met, and a total of 4 publications were presented from Oct 2007 – March 2008, one was accepted for publication in May 2008, while another one submitted for a workshop in June. The final system paper received an award at the prestigious SPIE International symposium on Medical Imaging 2008.

C KEY RESEARCH ACCOMPLISHMENTS

1. Completed all the data analysis from various phantom and patient trials.

D KEY TRAINING ACCOMPLISHMENTS

1. Training courses in medical imaging processing.

E REPORTABLE OUTCOMES

1. Presented 4 publications, as listed in the publications section (including three flagship conference publications in MICCAI), got one more accepted, and submitted another one.
2. A poster award at SPIE Medical Imaging 2008 for the proposed system in the PhD thesis.

F CONCLUSIONS

In conclusion, the system was exquisitely accurate in clinical trials and has shown usefulness. We require minimal alteration to the current clinical protocol or any significant increase in cost.

So what: The success of brachytherapy chiefly depends on our ability to intra-operatively cover the prostate with sufficient radiation while still avoiding excessive radiation to surrounding organs. Currently, such level of precision is not always achievable even by the most experienced physicians. Thus many implants fail or cause severe side effects owing to faulty seed placement, a problem what still cannot be corrected in the operating room. Our results indicate the feasibility of a system that could achieve intra-operative localization of the implanted seeds in relation to the prostate, to allow for in-situ dosimetric optimization and exit dosimetry. This ability to perform intra-operative dosimetry may change the standard of care in brachytherapy by allowing the physician to achieve technically excellent brachytherapy implants, resulting in improved disease control and quality of life for a large and steadily growing group of patients.

G PUBLICATIONS (List of publications in year 2 arising from the grant, sorted by publication date)

*G Chintalapani, **A Jain**, D Burkhardt, G Fichtinger: *CTREC: C-arm Tracking and Reconstruction using Elliptic Curves*. International workshop on Mathematical Methods in Biomedical Image Analysis, Alaska, June 2008. (Submitted)

*J Lee, X Liu, **A Jain**, J Prince, G Fichtinger: *Tomosynthesis-based radioactive seed localization in prostate brachytherapy using modified distance map images*. IEEE International Symposium on Bio-medical Imaging, May 2008, Paris. (Accepted).

***A Jain**, A Deguet, I Iordachita, G Chintalapani, J Blevins, Y Le, E Armour, C Burdette, D Song, G Fichtinger: *Detection of Intra-operative Edema in Prostate Brachytherapy*. SPIE Medical Imaging Feb 2008.

A Jain, A Deguet, I Iordachita, G Chintalapani, J Blevins, Y Le, E Armour, C Burdette, D Song, G Fichtinger: *Intra-operative Guidance in Prostate Brachytherapy Using an non-isocentric C-arm*. Tenth International Conference on Medical Image Computing and Computer-Assisted Intervention (MICCAI), Oct 2007 (Presented)

X Liu, **A Jain**, G Fichtinger: *Prostate Implant Reconstruction with Discrete Tomography*. Tenth International Conference on Medical Image Computing and Computer-Assisted Intervention (MICCAI), Oct 2007. (Presented)

Labat C, **A Jain**, G Fichtinger, J Prince: *Toward optimal matching for 3D reconstruction of brachytherapy seeds*. Tenth International Conference on Medical Image Computing and Computer-Assisted Intervention (MICCAI), Oct 2007. (Presented)

* - indicates publication solely produced from Oct 2007 – March 2008.

CTREC: C-arm Tracking and Reconstruction using Elliptic Curves

Anonymous CVPR submission

Paper ID ****

Abstract

C-arm fluoroscopy is ubiquitous in contemporary surgery, but it lacks the ability to accurately reconstruct three-dimensional information, attributable to the difficulty in obtaining the pose of X-ray images in 3D space. We propose a unified mathematical framework to address the issues of intra-operative pose estimation, correspondence and reconstruction, using simple elliptic curves. In contrast to other fiducial-based tracking methods, our method uses a single ellipse to constrain 5 out of 6 degrees of freedom of C-arm pose, along with randomly distributed unknown points in the imaging volume (either naturally present or induced by randomly placed beads or other markers in the image space) from two images/views to completely recover the C-arm pose. Preliminary phantom experiments indicate an average C-arm tracking accuracy of 0.51° and 0.12° STD. The method appears to be sufficiently accurate and appealing for many clinical applications, since it uses a simple elliptic fiducial coupled with patient information and has very minimal interference with the workspace.

1. Introduction

C-arm fluoroscopy is the most commonly used intra-operative imaging modality because of its low cost and ease of use, but it currently lacks the ability for robust and easy quantitative guidance. For intra-operative quantitative analysis, one needs to address the issues of 1) image distortion; 2) calibration of imaging parameters; 3) pose estimation; and 4) registration to other imaging modalities. The first two problems are well studied in literature and several solutions have been proposed to date [1, 14, 16]. On the other hand, pose recovery on unencoded mobile C-arms is still a major technical problem that presently does not have a practical solution in many areas of application. Adding to the problem is the non-isocentric nature of C-arms, where the two axes of rotation does not intersect. Also, it has been observed that calibration parameters, for both distortion and image, change from pose to pose, making it even harder to achieve accurate pose recovery.

To date, a wide variety of approaches have been proposed to recover C-arm pose, ranging from external tracking devices [12, 13], precise calibration fiducials consisting of beads, lines, conics etc in known geometry [3, 6, 11, 15, 16], to image-based pose estimation methods [5, 9] adapted from the computer vision literature. Auxiliary tracking devices are expensive and need an extra calibration step, optical systems have line of sight problems and electromagnetic trackers suffer from distortion from metallic instruments, thus adding to the complexity of the operating room.

Radio-opaque fiducials placed in the field of imaging have been demonstrated to be capable of achieving reasonable accuracies. However, these fiducials need to be manufactured and segmented precisely and the accuracies depend on the size of the fiducial, the number of features and the type of features, adding to the segmentation and imaging volume problems. It has been shown that ellipses serve as ideal features as a 3D ellipse would project as a closed ellipse in the 2D images [4, 8]. A circle is a special case of ellipse and has been used widely for pose estimation, either alone or with other features [2, 7, 10].

In image-based methods, point correspondences across the images, without the knowledge about their 3D locations, offer very strong constraints for determining the C-arm pose, popularly known as bundle adjustment in computer vision parlance[1]. Jain *et al.* proposed a mathematical framework to solve for pose parameters, point correspondences, and reconstruction using a high dimensional non-linear optimization with point features from three images [1]. It can be noticed that there is a trade-off between the number of points and the number of images used to determine the pose accurately. Determining correct point correspondences depends on the number of points, spacing between the points, configuration of the points and also on the number of images to eliminate degenerate matches. At the same time, increasing the number of images adds to the complexity of the non-linear optimization problem. While some procedures may be more tolerant to these shortcomings, despite pressing clinical needs, better approaches to achieve intra-operative quantitative fluoroscopy that fits

the existing clinical workflow are needed, thereby providing motivation for this work.

In this paper, we propose a unified framework to couple fiducial-based techniques with image-based algorithms to effectively determine C-arm pose from two or more images. We are using a single ellipse as our fiducial because ellipses serve as excellent 3D marker owing to their constrained mathematical framework and superior image segmentation, as reported in [1]. We present a detailed mathematical framework to recover pose using a known 3D ellipse and its 2D projective images. Our mathematical analysis shows that the ellipse from a single image offers symmetric solutions and hence can only constrain 5 out of 6 degrees of freedom. To recover all 6 degrees of freedom, we impose more constraints in the form of point correspondences across multiple images. It can be argued that these extra constraints can be obtained by adding more features to the elliptic fiducial for example a BB, a line, or even a second ellipse. Adding more features increases the burden of segmentation, interference with the anatomy and also creates a need for precise manufacturing and extra hardware in the operating room. Instead, we propose to use multiple projections and feature/point correspondences across these images to recover the pose, thereby using patient anatomical information as part of the fiducial. This is a novel method which benefits from both fiducial based methods and image based methods as the fiducial provides a good initial estimate for the point correspondences and the point correspondences in turn resolve the degenerate cases from the single ellipse.

We are targeting two pertinent applications for this work: 1) brachytherapy and 2) orthopaedics. Prostate brachytherapy is a procedure where radio-active seeds are implanted into the prostate to treat prostate cancer. C-arm fluoroscopy is used to get real-time dose analysis in the operating room [2]. Our framework fits well into this procedure as the ellipse has very minimal interference with the anatomy and at the same time we can also use the radioactive seeds as our point features to accurately determine the C-arm pose. Moreover, in orthopaedic applications, it is very common to insert screws, surgical markers etc., that can serve as our point fiducials. In applications that do not have many point features, one can either induce some markers or identify homologous landmark features in the projection images and use them as fiducials. All things considered, we believe that this combined approach has great potential for intra-operative C-arm tracking that would fit very well into existing clinical scenarios.

2. Method

The main components of this problem are: 1) c-arm pose and 2) point correspondences. It is assumed that the points

have been segmented from the X-ray images. C-arm imaging is typically approximated as a 5-parameter pinhole perspective projection camera [3, 4, 5] to be calibrated intra-operatively for each individual image. Recently, however, it has been shown that precise C-arm calibration does not significantly improve pose reconstruction, especially the relative pose between the images [6]. We assume constant calibration across the images, along with known pixel sizes. We present a detailed framework to estimate C-arm pose using two images, though this framework can be easily extended to three or more images.

2.1. Pose Estimation using Single Ellipse

Given a known 3D ellipse, the goal here is to estimate the pose of this ellipse from its corresponding projective images. It is typical to represent the segmented 2D ellipse as an equation of the form:

$$Au^2 + Bu + Cu^2 + Du + Fv + G = 0 \quad (1)$$

in each image, in which u and v are respectively the coordinates along the x and y axis of the image, measured in pixels, and A, B, C, D, F , and G are constants determined by the segmentation algorithm. It can be observed that this correlates with the general equation of a conic, the origin of which is sitting at the principal point. The equation of such a cone will appear like

$$A_0x^2 + B_0xy + C_0y^2 + \frac{D_0}{f}xz + \frac{F_0}{f}yz + \frac{G_0}{f^2}z^2 = 0. \quad (2)$$

where x, y, z are coordinates in a frame that has the focal point of the x-ray device as origin with z axis perpendicular to the image plane and x and y axis parallel to the imaging plane, and f is the focal length of the imaging scenario. This equation can be represented in matrix form as

$$\begin{bmatrix} x & y & z \end{bmatrix} \begin{bmatrix} A_0 & \frac{B_0}{2} & \frac{D_0}{2f} \\ \frac{B_0}{2} & C_0 & \frac{F_0}{2f} \\ \frac{D_0}{2f} & \frac{F_0}{2f} & \frac{G_0}{f^2} \end{bmatrix} \begin{bmatrix} x \\ y \\ z \end{bmatrix} = 0. \quad (3)$$

which can also be represented as

$$XM_0X^T = 0. \quad (4)$$

We broke the process into several steps using a method similar to that described for the case of a circle by Costa and Shapiro [7] and the detailed derivation can be found in [8]. We assume for simplicity that the coordinate frame of the 3D ellipse has the x -axis along its major axis, the y -axis along its minor axis, and the origin in the center of the ellipse. The first step involves finding the rotation between the coordinate frame defined by the image plane and the base coordinate frame of the cone itself (with x and y axes along

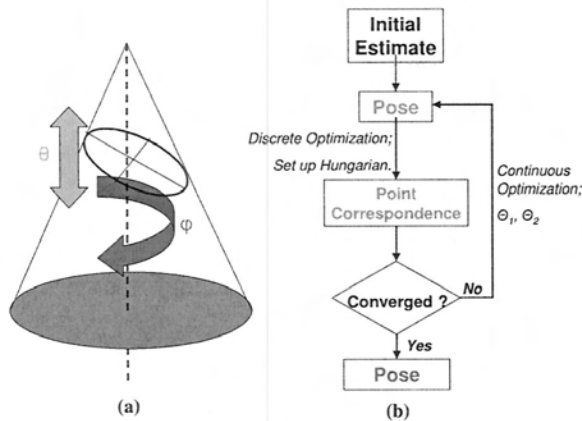


Figure 1. Graphical representation of the angles phi and theta, used to slice the cone and obtain an ellipse(left). Algorithmic flowchart showing pose estimation with point correspondences (right)

the major and minor axis of the cone and z axis along the cone's center). Note that the rotation matrix that achieves this transformation is just the eigenvectors of the original cone matrix M_0 . The base frame of the cone is of particular interest because in it the cone equation has special form of the type

$$\begin{bmatrix} x & y & z \end{bmatrix} \begin{bmatrix} A_B & 0 & 0 \\ 0 & C_B & 0 \\ 0 & 0 & \frac{G_B}{f^2} \end{bmatrix} \begin{bmatrix} x \\ y \\ z \end{bmatrix} = 0 \quad (5)$$

The next step is to find the transformation between the coordinate frame of the base cone and that of the 3D ellipse. By applying the constraints imposed by the physical size of the ellipse, we attempt to evaluate the set of transformations that would achieve this for a given image. We parameterize the problem by defining two values, ϕ and θ which together can represent a rotation from the base frame (z -axis aligned with the cone) to an arbitrary frame. To model this transformation, the base frame is first rotated by ϕ about its z axis and then by θ around the new y -axis. This transformation is illustrated in Figure 1a.

For any image, there are infinitely many possible (ϕ, θ) combinations, corresponding to infinitely many physical ellipses that could generate the observed projected ellipse in the X-ray image. These rotations can be expressed by the following matrices:

$$R_\phi = \begin{bmatrix} \cos \phi & -\sin \phi & 0 \\ \sin \phi & \cos \phi & 0 \\ 0 & 0 & 1 \end{bmatrix} \quad (6)$$

$$R_\theta = \begin{bmatrix} \cos \theta & 0 & \sin \theta \\ 0 & 1 & 0 \\ -\sin \theta & 0 & \cos \theta \end{bmatrix} \quad (7)$$

Our goal therefore is to solve for ϕ and θ such that:

$$X R_\phi R_\theta M_P R_\theta^T R_\phi^T X^T = 0 \quad (8)$$

where M_P is the equation for the cone in its base frame.

Furthermore, note that all parallel planes slicing the cone, create a conic curve with the exact same eccentricity. In our case, this eccentricity should be equal to the eccentricity of the 3D ellipse (a known constant). So without loss of generality, if we set $Z = 1$, we will get the equation of an ellipse, such as

$$A_P * x^2 + B_P * xy + C_P * y^2 = K \quad (9)$$

where

$$A_P = G_0 \sin^2 \theta + C_0 \cos^2 \theta \sin^2 \phi + A_0 \cos^2 \theta \cos^2 \phi \quad (10)$$

$$B_P = 2\{-A_0 \cos \theta \cos \phi \sin \phi + C_0 \cos \theta \sin \phi \cos \phi\} \quad (11)$$

$$C_P = A_0 \sin^2 \phi + C_0 \cos^2 \phi \quad (12)$$

The ellipse generated in this slice can also be described by a more common equation:

$$\frac{(x \cos \psi + y \sin \psi)^2}{a^2} + \frac{(x \sin \psi - y \cos \psi)^2}{b^2} = K \quad (13)$$

where ψ is a rotation around the z -axis of the 3D ellipse, a & b are the major & minor axes of the 3D ellipse. K will be scale-constant dependent on the z value at which the slice was taken. Expanding this equation simplifies to

$$\left(\frac{\cos^2 \psi}{a^2} + \frac{\sin^2 \psi}{b^2}\right) x^2 + \sin 2\psi \left(\frac{1}{a^2} - \frac{1}{b^2}\right) xy + \left(\frac{\sin^2 \psi}{a^2} + \frac{\cos^2 \psi}{b^2}\right) y^2 = K \quad (14)$$

So, from equation 9, we know that for some angle of rotation ψ :

$$A_P = \left(\frac{\cos^2 \psi}{a^2} + \frac{\sin^2 \psi}{b^2}\right)$$

$$B_P = \sin 2\psi \left(\frac{1}{a^2} - \frac{1}{b^2}\right)$$

$$C_P = \left(\frac{\sin^2 \psi}{a^2} + \frac{\cos^2 \psi}{b^2}\right)$$

Combining these equations to eliminate ψ and K , gives us

$$\begin{aligned} A_P + C_P &= K \left(\frac{1}{a^2} + \frac{1}{b^2}\right) \\ (A_P - C_P)^2 + B_P^2 &= K^2 \left(\frac{1}{a^2} - \frac{1}{b^2}\right)^2 \\ \Rightarrow \frac{(A_P - C_P)^2 + B_P^2}{(A_P + C_P)^2} &= \frac{\left(\frac{b^2}{a^2} - 1\right)^2}{\left(\frac{b^2}{a^2} + 1\right)^2} \end{aligned}$$

Note that if we were imaging a circle, the right hand term reduces to 0, indicating $B_P = 0$, and $A_P = C_P$. Substituting the values for A_P , B_P , and C_P previously presented in equations 10, 11, 12 allows us to obtain an equation relating θ to ϕ . This equation is a quadratic equation in $\cos^2(\phi)$ of the form, with the $K_n(\theta)$ functions of θ :

$$K_1(\theta) \cos^4 \phi + K_2(\theta) \cos^2 \phi + K_3(\theta) = 0 \quad (15)$$

Since equation 15 is a bi-quadratic equation in $\cos \phi$, for any given value of θ there are 8 values of ϕ in general that satisfy the constraint that it imposes. Moreover, observe that if ϕ ($0 \leq \phi < \pi/2$) is a solution, then $\pi - \phi$, $-\pi + \phi$ & $-\phi$ are also solutions. These would correspond to the 4 symmetric solutions owing to the inherent symmetry in the cone and the ellipse. Furthermore, ϕ and $-\pi + \phi$ correspond to the same ellipse sitting in exactly the same position. In many cases, some solutions for ϕ would be imaginary when $|\cos \phi| > 1$, meaning that there is no feasible ellipse for that given θ .

At this stage, we have constrained the solution space of the ellipse/C-arm pose, reducing the 6-dimensional pose-parameter space to a function of a single parameter ϕ/θ . With respect to the ellipse frame, there are eight symmetric locations of the X-ray source, all of them being reflections along the x - y , y - z and z - x planes. The other eight solutions have the same position of the X-ray source, but the image rotated by π along the center line of each 3D cone. Thus it can be observed that, with respect to the ellipse, all the feasible pose solutions lie on 8 non-intersecting closed curves parametrized by ϕ/θ .

Given a (ϕ, θ) combination, to obtain the third rotation angle ψ we apply the following transformation to our coordinate frame, giving us a cone of the form

$$X R_\phi R_\theta M_P R_\phi^T R_\theta^T X^T = X C_E X^T = 0 \quad (16)$$

where C_E is the cone equation in a coordinate frame aligned with the frame of the 3D ellipse, and a rotation of ψ along its z -axis. We next apply a rotation by the angle ψ to bring the x and y axes of our coordinate system parallel to the major and minor axes of the real ellipse. Solving the equation, this angle is given by

$$\psi = 1/2 * \arctan(2 * B_E / (C_E - A_E)) \quad (17)$$

The rotation transformation of ψ along the z -axis can be described as

$$R_\psi = \begin{bmatrix} \cos \psi & -\sin \psi & 0 \\ \sin \psi & \cos \psi & 0 \\ 0 & 0 & 1 \end{bmatrix} \quad (18)$$

The coordinate system created by the combination of these rotations now has axes parallel to the axes of the 3D ellipse, but is centered at the imaging focal point. The final step

therefore, is to compute the translation required to bring the center of the frame to the center of the ellipse. This translation is computed by taking a slice of the cone at distance f away from the center, computing its major axis at this point. Equating the computed length of the major axis as a function of f , to the known value, provides f . The coordinate system is then translated by this vector.

Combining these transformations allows us to create an algorithm to determine the set of possible poses that could have created a given image. However, as infinitely many possible (ϕ, θ) combinations exist, the ellipse image cannot be used to uniquely determine the pose. It constrains 5 of the 6 degrees of freedom of pose, allowing a single degree of freedom that must be removed through further constraints.

2.2. Combined Mathematical Framework

As shown above, a single ellipse from each projection image returns the pose in (ϕ, θ) space with 8 degenerate poses, i.e., the projection of the known 3D ellipse in any of these poses would result in exactly the same 2D image. In order to eliminate these degenerate cases, we propose to impose more constraints in the form of point correspondences across images. Even though the projections of the 3D ellipse are identical, the projections of the 3D point clouds differ and hence provides us with extra constraints to break the symmetry as shown below.

Let N_m be the number of points identified in images I_m with pose $[R_m, T_m]$, θ_m be the corresponding solution space for C-arm pose using ellipse from image I_m and projection model M_m . Let s_{lm} be the position of l^{th} segmented point in m^{th} image. When two images are used, the optimization problem can be formulated as follows:

$$\arg \min_{\theta_1, \theta_2, f} \sum_{i=1}^{N_1} \sum_{j=1}^{N_2} C_{ij} f_{ij}$$

where

$$\sum_{j=1}^{N_2} f_{ij} \geq 1 \forall i; \sum_{i=1}^{N_1} f_{ij} \geq 1 \forall j; f_{ij} \in \{0, 1\} \quad (19)$$

and C_{ij} is the the cost of matching point p_{i1} to points p_{j2} . Note that it varies with any variation in θ_1, θ_2 . f_{ij} is a discrete variable taking a value 1/0, and deciding the correctness of the match $\langle i, j \rangle$. The inequalities force every segmented point to be chosen at least once. Thus, f represents any feasible global match (and vice versa), with the cost of that correspondence given by $\sum \sum C_{ij} f_{ij}$. The problem hence is to compute θ_1, θ_2, f that minimize the total cost. It should be noted that since the images represent

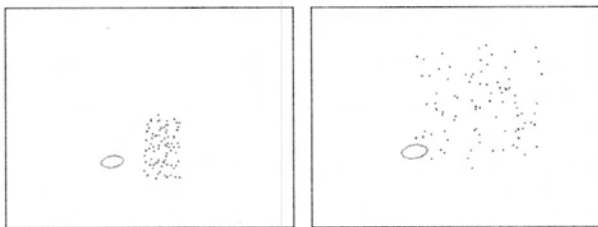


Figure 2. Simulated point clouds along with ellipse fiducial for prostate brachytherapy and orthopaedic procedures

a real situation, this optimization has a solution with a near-zero cost. The procedural flow diagram is shown in Figure 1b. For each θ_i , there are eight ϕ_i symmetric solutions and hence we evaluate the objective function 64 times for two images to eliminate the degenerate cases. The number of evaluations can be decreased by tailoring the algorithm to be application dependent or by constraining the motion of the C-arm etc. The basic idea is that at global optimum, correct pose would invoke correct correspondences and these correspondences would converge to the optimal pose. At any other point in the solution space, incorrect pose would lead to inconsistent correspondences and hence by iteratively solving for both pose and point correspondences, a unique global solution can be achieved.

In general, any cost metric that globally measures the deviation from the observation, should perform well. We use projection error as our cost metric. This projection error can be computed as the L_2 norm of the projection of the 3D points (computed by intersecting the rays from the corresponding 2D points in the X-ray image to its source) on to the 2D images. Once the cost matrix is computed, we use traditional Hungarian assignment method to solve for optimal point correspondences [1].

3. Experiments and Results

Simulation Studies: Two types of synthetic data, one for prostate brachytherapy and the other for orthopaedic applications, were created to evaluate our algorithm. Both the simulation software and the algorithm were implemented in MATLAB. For two images, the algorithm takes about 20-60 seconds depending on the number of points used, with typical convergence in 2-3 iterations. The C-arm imaging parameters for both the simulations are: focal length = 1000 mm; pixel size = 0.44 mm/pixel; image size = (512, 640); and origin = (256, 320); The diameter of the 3D ellipse was fixed at 18 inches. For prostate brachytherapy simulations, we created 5 datasets, each dataset has 6 images taken at regular intervals along a 20° cone. We varied the imaging volume from 40cc to 60cc in increments of 5cc. For orthopaedic data, we varied the imaging volume from 100cc to 1000cc in increments of 100cc. We divided the experiments into three separate cloud sizes: *sparse*, *medium*, and

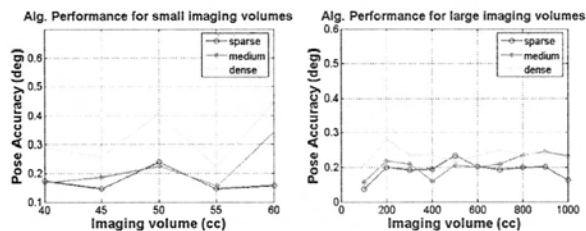


Figure 3. Relative pose error as a function of the imaging volume for small volumes (left) and large volumes (right)

dense clouds consisting of at least 10-15, 20-30, and 70-80 points respectively. These point clouds were chosen randomly for 5 iterations. Figure 2 shows an example simulated image with ellipse and point clouds. We believe that this data represents the spectrum of different types of surgical scenarios including brachytherapy and orthopaedic procedures.

Figure 3 shows the simulation results for small and large imaging volumes. Each datapoint is an average of $5 \times \binom{6}{2} \times 5 = 375$ runs. Pose recovery accuracy varies with the size of the point cloud, average being about 0.34° for small volumes and 0.2° for large volumes. Although, the variation is not much significant with the large volumes because of the wide distribution of the feature points. These results show that when there is no error in the data, pose can be recovered accurately.

We are currently exploring the sensitivity of the algorithm to the segmentation errors from both ellipse segmentation and point segmentation. The overall failure rate for large imaging volumes has decreased from 10% to 0.1% when compared to the small imaging volumes. These simulation results show that our algorithm successfully converges to the optimal solution in case of large imaging volumes and small imaging volumes with sparse and medium data distribution and is near perfect (success rate of 95%) for small imaging volumes with dense data points. This can be attributed to the fact that the point mismatches are more prevalent in dense point clouds and hence are throwing off the convergence in the two image algorithm. We show an improvement in the performance by using partial information from the third image below.

Phantom Experiments: Experiments were performed on a brachytherapy phantom consisting of both the seeds and the FTRAC fiducial rigidly attached as shown in Figure 4. The cloud phantom comprises of multiple slabs, thus capable of multiple *random* point configurations. 100 points with 1.56 *points/cc* were used. X-ray images within a 20° cone around the AP-axis were *randomly* taken using a *Philips Integris V3000* fluoroscope and corrected for distortion. Thus both the seed locations and X-ray pose were not biased/optimized in any way, closely representing an

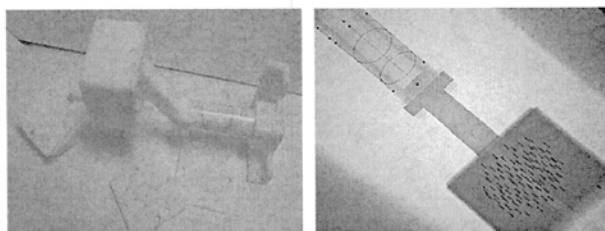


Figure 4. An image of the point phantom attached to the FTRAC fiducial (left). A typical X-ray image of the combination (right)

uncontrolled surgical scenario. Each image was hand segmented to establish the true segmentation and correspondence, thereby allowing for some segmentation error. The true C-arm pose and reconstruction was compared to that computed from the algorithm.

Figure 5.b shows the performance of the algorithm with respect to the number of points used along with the ellipse. Each datapoint is an average of $5 * \binom{6}{2} * 30 = 2250$ runs. For phantom data, as few as 4 – 5 points along with the ellipse are sufficient to accurately recover the pose (0.74°) and also are able to attain a success rate of 99%. The second set of phantom experiments involve taking multiple x-ray images and reconstructing the 3D seed locations from its corresponding 2D projection coordinates, for which accurate C-arm tracking is a must. For each phantom dataset, we have used sets of two images, determined the relative pose between these images and then reconstructed the 3D seed coordinates. Although this works perfectly on sparse data, our goal is to make it work on dense data such as brachytherapy seed data. The results are shown in Table 1. Note that the data in each cell is an average of 15 runs. Eventhough the average pose error is about (1°), only half of the seeds are correctly matched because of the reconstruction singularities introduced by using only two images, which is fully expected for dense data.

To understand better, how information from the third image enhances the algorithm convergence, we have used a third image to identify the correct matches as valid correspondences between the points identified by points that create loops of size one. Given two images, I_1, I_2 , we select a third image I_3 and run the algorithm on sets of two images. Consider a point p_{i1} in image I_1 being matched to a point p_{j2} in image I_2 , and to a point p_{k3} in image I_3 . This match between p_{i1} to p_{j2} is considered a valid match if and only if p_{j2} matches p_{k3} . The pose estimation algorithm is run again using only these valid matches. We refer to this experiment as 2.5 images rather than 3 images in Table 1, since only partial information from the third image is used.

This added information from the third image has increased the matching rate to 90% with a better pose and reconstruction accuracy. The error for mismatched seeds is still high. The reason is that inspite of high matching

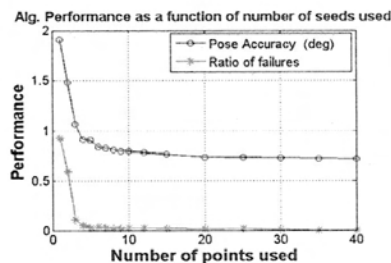


Figure 5. Performance as a function of number of points used along with the ellipse. Note that three to five points achieve 99% success rate.

rate and improved reconstruction accuracy, the projection of the solution using three images is not exactly the same as that of using two solutions. Although these accuracies are mostly acceptable, prostate brachytherapy needs 99% matching rate to determine the intra-operative dosage accurately, which can be achieved by extending our framework to use three images. The basic idea here would be to use two images to optimize the pose and then use three images to solve for matching iteratively. The theoretical complexity of using three or more images is similar to that of two images, except that the matching algorithm would be employing more sophisticated combinatorial checks like MARSHAL [1].

4. Discussion

A unified mathematical framework for C-arm tracking, point correspondences and reconstruction has been proposed, along with experimental validation on simulation and phantom studies. Our experiments indicate an average accuracy of 0.51° in orientation, with a STD of 0.12° . The primary contribution of this work is the use of ellipse to determine pose with a combinatorial approach to establish point correspondences. We show that the projection of elliptic curves constrains 5 out of the 6 degrees of freedom of the C-arm pose. Furthermore it can also recover the 3D scale of the reconstruction. To completely recover the true C-arm pose, our method uses constraints in the form of additional point correspondences from multiple images. We show that four or five additional correspondences can successfully recover the pose 99% of the time with an accuracy of 0.74° .

We have conducted our validation on randomly selected views and number/distribution of points, indicating the robustness of the algorithm to uniformity and reliability in performance. Though the alternatives of well designed calibration fixtures and image based procedures are also available, they become cumbersome and impractical, specifically when employed in the current clinical setup. We believe that the presented framework represents a significant step toward a complete pose reconstruction system employ-

	Number of Seeds									
	2 Images					2.5 Images				
	40	55	70	85	100	40	55	70	85	100
Pose Accuracy (deg)	0.81	1.01	0.95	1.37	0.80	0.49	0.42	0.56	0.59	0.48
Matching Rate (%)	63.38	62.42	53.04	40.94	45.20	94.16	90.25	90.14	88.57	89.37
Reconstruction Error (matches)(mm)	3.27	1.27	1.72	3.84	1.18	0.19	0.25	0.33	0.22	0.31
Reconstruction Error(mismatches) (mm)	26.25	34.96	35.41	31.04	33.04	0.63	5.04	5.19	6.38	6.06

Table 1. The algorithm's performance on phantom data. 2-image seed matching is completely erroneous (left), with over a quarter of the seeds being mismatched with high reconstruction error, yet low projection error and reconstruction accuracy. Adding just little information from a third image boosts performance (right). Most seeds match, though the reconstruction error is high for the few mismatched seeds.

ing very little external hardware and very minimal interference with the anatomy being imaged (one could think of a small ellipse attached to a wire frame into the field of view and imaged along with the patient). Moreover, our simulation results show that this method can be used for a variety of applications ranging from prostate brachytherapy (small imaging volume, dense point features) to orthopaedic applications (large imaging volume, sparse to medium point features).

We are currently performing more simulations to validate the sensitivity of the algorithm to segmentation errors and are also looking at measuring target registration error distribution of the point clouds. Efforts to validate our system on clinical prostate brachytherapy data are currently underway. Further extension of this approach to reconstruct points using three views could significantly improve the current clinical viability of intra-operative quantitative fluoroscopy, especially in brachytherapy.

References

- [1] D. Burkhardt, A. Jain, and G. Fichtinger. A cheap and easy method for 3D C-arm reconstruction using elliptic curves. In *Medical Imaging 2007: Visualization and Image-Guided Procedures*. Edited by Cleary, Kevin R.; Miga, Michael I.. *Proceedings of the SPIE, Volume 6509*, pp. 65090B (2007)., volume 6509 of *Presented at the Society of Photo-Optical Instrumentation Engineers (SPIE) Conference*, Mar. 2007. 2
- [2] M. Costa and L. Shapiro. 3d object recognition and pose with relational indexing. *CVIU*, 79(3):364–407, September 2000. 1, 2
- [3] R. Hofstetter, M. Slomczykowski, M. Sati, and L. Nolte. Fluoroscopy as an imaging means for computer-assisted surgical navigation. *Comput Aided Surg*, 4(2):65–76, 1999. 1, 2
- [4] R. Hu and Q. Ji. Camera self-calibration from ellipse correspondences. In *ICRA*, pages 2191–2196, 2001. 1
- [5] A. Jain and G. Fichtinger. C-arm tracking and reconstruction without an external tracker. In *MICCAI*, pages 494–502, 2006. 1, 2, 6
- [6] A. Jain, T. Mustufa, Y. Zhou, E. C. Burdette, G. Chirikjian, and G. Fichtinger. A robust fluoroscope tracking (frac) fiducial. *Med Phys*, 32(10):3185–98, Oct 2005. 1, 2
- [7] F. Kahl and A. Heyden. Using conic correspondence in two images to estimate the epipolar geometry. In *ICCV*, pages 761–766, 1998. 1
- [8] H. W. Kuhn. The Hungarian method for the assignment problem. *Naval Research Logist. Quart.*, 2:83–97, 1955. 5
- [9] Y. Ma and et al. *An Invitation to 3-D Vision*. Springer, 2000. 1
- [10] P. K. Mudigonda, C. V. Jawahar, and P. J. Narayanan. Geometric structure computation from conics. *Lancet. Oncol.*, 4:233–241, 2002. 1
- [11] N. Navab, A. Bani-Hashemi, M. Mitschke, D. W. Holdsworth, R. Fahrig, A. J. Fox, and R. Graumann. Dynamic geometrical calibration for 3-d cerebral angiography. In *SPIE Medical Imaging*, pages 361 – 70, Feb 1996. 1
- [12] OEC 9800 FluoroTrak™. GE Healthcare, Waukesha, WI. 1
- [13] StealthStation®. Medtronic Surgical Navigation Technologies, Louisville, CO. 1
- [14] T. Tang. Calibration and point-based registration of fluoroscope images. Master's thesis, Queen's University, Jan 1999. 1, 2
- [15] Z. Yaniv and L. Joskowicz. Precise robot-assisted guide positioning for distal locking of intramedullary nails. *IEEE Trans Med Imaging*, 24(5):624–35, May 2005. 1
- [16] J. Yao, R. H. Taylor, R. P. Goldberg, R. Kumar, A. Bzostek, V. R. Van, P. Kazanzides, and A. Guezic. A c-arm fluoroscopy-guided progressive cut refinement strategy using a surgical robot. *Comput Aided Surg*, 5(6):373–90, 2000. 1, 2

TOMOSYNTHESIS-BASED RADIOACTIVE SEED LOCALIZATION IN PROSTATE BRACHYTHERAPY USING MODIFIED DISTANCE MAP IMAGES

Junghoon Lee¹, Xiaofeng Liu², Ameet K. Jain^{2,3}, Jerry L. Prince¹, Gabor Fichtinger^{2,4}

Johns Hopkins University

¹Department of Electrical and Computer Engineering and ²Computer Science, Baltimore, MD, USA

³Philips Research North America, Briarcliff, NY, USA

⁴Queen's University, School of Computing, Canada

ABSTRACT

We have developed a tomosynthesis-based radioactive seed localization method for prostate brachytherapy. In contrast to the projection image-based matching approach, our method does not involve explicit segmentation of seeds and can recover hidden seeds. Modified distance map images are computed from a limited number of x-ray projection images, and are backprojected to reconstruct a 3-D volume of interest. Candidate seed locations are extracted from the reconstructed volume and false positive seeds are eliminated by solving an optimal geometry coverage problem. The simulation results indicate that the implanted seed locations can be estimated from three or four images depending on the number of seeds if the pose of a C-arm is known. The algorithm was validated using phantom and clinical patient data.

Index Terms— Tomosynthesis, prostate cancer, brachytherapy, modified distance map.

1. INTRODUCTION

Prostate cancer is one of the most leading cancers in men in the United States with 218,890 new cases and 27,050 deaths annually. However, it can be fully treated if detected early [1]. Brachytherapy is a definitive treatment for low risk prostate cancer, which involves permanent implantation of radioactive seeds into the prostate. Its success mainly depends on the ability to implant a sufficient number of seeds to ensure that the target gland is treated with a therapeutic dose while sparing adjacent healthy structures (e.g. rectum, urethra, nerve bundles) from excessive radiation. Typically, an implantation plan is made preoperatively based on idealistic seed patterns and an ultrasound volume study. However the actual implant procedure introduces errors due to various reasons including patient motion, deviation of the needle, and prostate swelling. In order to overcome these limitations, intraoperative planning under the guidance of ultrasound and fluoroscopy was proposed.

There are various computational tools available to localize the seeds from a limited number of x-ray images. Three-dimensional coordinates of the implanted seeds can be calculated from multiple x-ray images upon resolving the correspondence of seeds [2, 3, 4, 5, 6, 7, 8, 9, 10]. These methods require accurate segmentation and identification of the seeds in all x-ray projection images followed by solving matching problem between identified seeds in different projection images. Incorrect localization of the seeds will cause undetected seeds in 3-D reconstruction. Since typically up to 7% of the

seeds can be hidden in the x-ray images [8], it is hard to perfectly identify the seeds in all images even if sophisticated segmentation and labeling methods are used. The unidentified seeds are usually recovered manually, which is time consuming and sometimes requires extra x-ray images. It is sometimes impossible to recover them when seeds are hidden.

Tutar *et al.* [11] proposed a modified tomosynthesis technique, so called selective back projection which requires large number of images (≥ 7) and large angle separation ($\geq 25^\circ$). Also, it is prone to introduce false positive (FP) seeds and to miss true seeds when there are C-arm pose estimation errors (Sec. 2.1 describes the reason why pose estimation of the C-arm is necessary). Their FP removal process based on the detected seed size is also vulnerable to the pose errors since these errors affect the size of the detected seeds. A discrete tomography algorithm based on a distance map was previously developed [12]. However, some seeds (especially seeds that are in a sparse seed region) were undetected when it was applied to the clinical patient data in which seeds were smaller than those in the phantom used in [12] and pose errors were introduced. These algorithms were tested only on simulation and phantom data, but not on clinical patient data.

In order to make the reconstruction more robust to the pose and the calibration errors, we developed a tomosynthesis-based seed localization method using shape control function-based modified distance map images. We solve a reduced optimal coverage problem to remove the FP seeds. The proposed method was tested on simulation and phantom data, and was applied to two clinical patient data sets.

2. MATERIALS AND METHODS

Figure 1 shows an example that can be encountered when we reconstruct the seeds using tomosynthesis. Three seeds (solid circles) are projected to three images and these three images are backprojected to reconstruct a 3-D volume. From the reconstructed volume, five candidate seeds are detected and they appear to be legitimate in every image. The problem is to eliminate two FP seeds and detect three true seeds correctly. The intuition is that each seed mark in every image must be covered by at least one of the candidate seeds. In this simple example, there will be seed marks in one or more images to which no seed in the volume is projected if we eliminate any of the true seeds. Starting from this intuition, we have developed a theoretical framework based on optimal geometry coverage. In order to make the reconstruction more robust to the pose and calibration errors, we use a modified distance map image instead of using the projection image itself. We now describe the algorithm in detail.

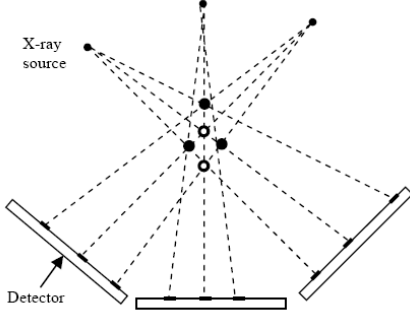


Fig. 1. Example tomosynthesis geometry.

2.1. Image acquisition, calibration and distortion correction

X-ray projection images are acquired from a C-arm with a limited angle separation, e.g. $\leq 20^\circ$ due to the limited space in the operating room near the patient. The acquired images are dewarped and calibrated (previously) by using a calibration phantom. Since C-arms in most facilities do not have encoded rotational joints and they may move on wheels between shots, we need to determine the pose of the C-arm using tracking devices. We use a fluoroscope tracking (FTRAC) fiducial which is a radiographic fiducial system creating a unique projection image from each direction [13].

2.2. Seeds segmentation and modified distance map image computation

Once (distortion corrected) projection images are acquired, the seed cloud region is selected by user-driven morphological operators and then seed-only images are computed. Since the background is highly nonuniform in actual patient images, the nonuniform background is first extracted by dilation and then subtracted from the original image. Binary seed-only images are computed from the background subtracted images by adaptive thresholding. For each seed-only image, a distance map is computed using a distance transform which computes the Euclidean distance between each pixel and its nearest seed region. Since we do not need to identify all seeds in the 2-D images, overlapping seeds are simultaneously considered to be at zero distance. Then the modified distance map images are computed using a shape control function from the distance maps. In this paper, we use an unnormalized gaussian as a shape control function:

$$I(\mathbf{x}) = e^{-d(\mathbf{x})^2/2\sigma^2} \quad (1)$$

where $I(\cdot)$ is the modified distance map image, $\mathbf{x} \in \mathbb{R}^2$ is the pixel location in the image, d is the distance map of the image, and σ^2 is the variance which controls the tapering speed. The pixel value inside the seed regions is 1 and the pixel value tapers down as the distance between the pixel and the nearest seed region increases. σ^2 is determined depending on the pose estimation errors. The intuition of this approach is that the seed regions in the seed-only image are not exact due to the pose and calibration errors and the probability that a pixel belongs to the seed region is related to the distance between that pixel and its nearest seed region. A pixel closer to the seed region in the seed-only image has higher probability that it belongs to the true seed region, but a pixel far apart from the seed region in the seed-only image has small probability that it belongs to the true seed region.

2.3. Volume reconstruction and candidate seeds extraction

A 3-D volume is reconstructed using backprojection, which is equivalent to a generalized form of tomosynthesis for arbitrary orientations. A global reference coordinate system (FTRAC coordinate system) is defined and a local coordinate system (C-arm coordinate system) is defined with respect to the global reference coordinates. 3×4 projection matrix which maps a point in 3-D space to the corresponding projection point in the projection image at each pose is computed from the 4×4 transformation between the global reference and the local coordinates and the perspective projection of the C-arm. The projection matrices are used for both reconstruction and cost computation for FP seeds removal. After the 3-D reconstruction, candidate 3-D seeds are extracted by thresholding. Unlike a reconstruction from actual projection images, the reconstructed voxels take values between 0 and 1 due to the nature of the modified distance map images, and the threshold varies within a small range, e.g. 0.9–1.0, which makes an automatic thresholding based on the average size and the number of detected candidate seeds possible. The thresholded 3-D seed regions are labeled using connected component labeling method and the centroid of each labeled candidate seed region is computed by averaging the 3-D coordinates of the voxels in each seed region.

2.4. False positive seeds removal

A tomosynthesis-based approach is prone to introduce FP seeds. Therefore an FP seed elimination process from the candidate seeds is necessary. This problem is solved as a reduced optimal geometric coverage problem as was done in [12], and a detailed description is followed for the completeness of the paper.

The goal in this process is to find the N_t true seeds from N_c candidate seeds such that all the 2-D seed regions are covered in all projection images. Since an FP seed is projected close to some true seeds in every image but true seeds are not projected close to the other true seeds in all the images, a cost function of a given seed can be defined as the sum of the closest distances between the projections of this seed and the projections of all the other true seeds in all images. However, since this optimal coverage problem is NP-hard [14] and it requires impractical amount of time for a large number of seeds, a greedy search to minimize local costs rather than the global cost is adopted to reduce the computational burden.

To ensure that the projections of selected true seeds cover all the 2-D seed regions in all seed-only images, all 2-D seed regions in all seed-only images are labeled using connected component labeling method and the candidate seeds are clustered based on their projections in each labeled seed-only image. The purpose of the seed labeling is not to segment the 2-D seed regions or to identify the number of true seeds in each image, so the overlapped seed regions will be labeled as one. This clustered seed labels are used for the coverage function minimization.

All candidate seeds are first projected onto each image. Let x_n be a 3-D candidate seed position and P^i be a projection matrix for the i^{th} projection image. Then the projection of x_n to the i^{th} image becomes $P^i x_n$. Let $L^i(x)$ be a label corresponding to a point x , then the label of a projection of a 3-D seed position x_n in the i^{th} image becomes $L^i(P^i x_n)$. The projections of all candidate seeds in the i^{th} image are clustered as sets $\Omega_k^i = \{x_n | L^i(P^i x_n) = k\}$, $k = 1, 2, 3, \dots, K^i$ where K^i is the number of labels in the i^{th} labeled seed-only image. The seed region with label k in i^{th} image is covered by $|\Omega_k^i|$ seeds where $|\Omega_k^i|$ is the cardinal of set Ω_k^i and $|\Omega_k^i| \geq 1$. If a seed region is covered by only one seed, i.e. $|\Omega_k^i| = 1$, this seed must be a true seed because otherwise this

region cannot be covered. The set of such seeds can be described as:

$$\mathbf{G} = \cup_i \{x_n | L^i(P^i x_n) = k \text{ and } ||\Omega_k^i|| = 1, k = 1, 2, \dots, K^i\}, \quad (2)$$

for $i = 1, 2, \dots, N_p$ where N_p is the number of projection images. The optimization problem can be reduced to choose $(N_t - ||\mathbf{G}||)$ seeds from $(N_c - ||\mathbf{G}||)$ candidate seeds. And a local cost function is defined as:

$$C(x_n) = -\sum_{i=1}^{N_p} \frac{1 + D^i(x_n)}{1 + d_n^i}, \text{ for } x_n \in (\mathbf{S} - \mathbf{G}) \quad (3)$$

$$D^i(x_n) = \min_{m \neq n} ||P^i x_m - P^i x_n||, \text{ for } x_m \in \mathbf{S}$$

where \mathbf{S} is a set of candidate seeds, and d_n^i is the distance from the projection of x_n to the nearest seed region in the i^{th} image. d_n^i is included in the cost function to reflect the effect of imperfect pose estimation. This problem is solved using greedy search iteratively. During each iteration, a seed that has the largest cost value computed by (3) is considered as an FP seed and is removed from \mathbf{S} and \mathbf{G} is updated at each iteration if there are additional seeds which cover some seed regions alone after removing one FP seed. Iteration continues until N_t seeds are left.

3. NUMERICAL RESULTS

3.1. Simulations

Simulation studies were conducted on synthetic projection images to evaluate the performance of our method. Three cases were considered for a 50 cc prostate: (1) seed density of 1.5 seeds/cc with 72 implanted seeds, (2) seed density of 2.0 seeds/cc with 96 implanted seeds, and (3) seed density of 2.25 seeds/cc with 112 implanted seeds. Three data sets were generated for each case. The focal length of the C-arm and the pixel size of the image were chosen to be 1000 mm and 0.44^2 mm^2 , respectively based on our experience. Each seed is represented by a cylinder with radius of 0.4 mm and length of 1.45 mm. In each data set, there are six images generated on a 20° cone around the AP axis. No C-arm pose error was introduced. 3-D reconstructions of the seeds are computed based on three and four images with a voxel size of 0.5^3 mm^3 . We have chosen three combinations of selecting three (or four) images out of six available images in each data set and computed nine reconstructions for each case (3 combinations \times 3 data sets). Since there was no pose error, σ was chosen to be small (e.g. 1 pixel = 0.5 mm) and threshold for localizing candidate seeds in 3-D reconstruction was chosen to be high (e.g. 1.0). The estimated seed positions were compared to the ground truth. The results are shown in Table 1 and imply that the implanted seeds can be localized with a detection accuracy of $> 98\%$ or $> 99\%$ from three or four images, respectively, depending on the number of seeds when there is no C-arm pose error.

3.2. Phantom experiments

Phantom experiments were performed on a seed phantom which was fabricated using acetol. The phantom consists of twelve slabs with thickness of 5 mm and each slab has at least a hundred holes with 5 mm spacing where seeds can be positioned. The FTRAC was precisely attached to the seed phantom in a known position. There was about $0.5^\circ - 1^\circ$ rotational error introduced in the attachment process which results in about 0.5 mm error in the ground truth seed locations. Three data sets were generated with the numbers of seeds of 42, 72, and 102 keeping seed density constant at about 1.56 seeds/cc

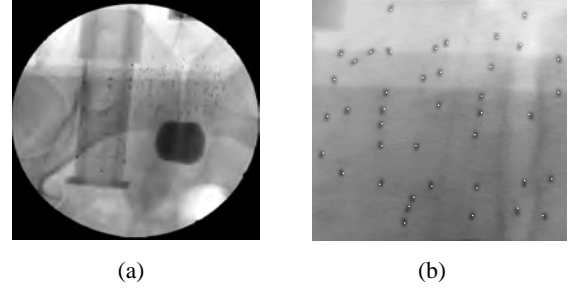


Fig. 2. (a) Example clinical patient image showing 66 seeds and FTRAC images. (b) The estimated seed centroids projected onto one of three projection images used for reconstruction.

for all three data sets. For each data set, six images were acquired within a 20° cone around the AP axis using a *Philips Integris V3000* fluoroscope and were dewarped using previously acquired calibration phantom data. Four, five, and six images were selected from the six available images in each data set based on the residual errors provided by the FTRAC software, and were used for 3-D reconstructions. The voxel size of the 3-D reconstructions was 0.5^3 mm^3 . Considering the pose errors, σ was chosen to be larger (e.g. 3 pixels = 1.5 mm) and the threshold for localizing candidate seeds in 3-D reconstruction was chosen to be smaller (e.g. 0.95) than the values chosen for simulations. The estimated seed positions were compared to the ground truth, and the results are shown in Table 2. The results imply that the implanted seed locations can be estimated with a detection accuracy of $> 97\%$ from five projection images.

3.3. Clinical experiments

The proposed method was applied to two clinical patient data sets. X-ray images were taken within a 10° cone around the AP axis using *OEC 9800* fluoroscope, and were dewarped and calibrated using calibration phantom data acquired prior to the surgery. The FTRAC from which the pose of the C-arm at each image was estimated was precisely attached to the needle insertion template in a known position. 61 and 66 ^{103}Pd seeds were implanted into 30 cc prostate and the size of the seed was 4.92 mm (length) and 1.0 mm (radius) with radio-opaque size of about 1.45 mm (length) and 0.8 mm (radius). Three images were selected from the acquired images (10 images for 61 seeds, 9 images for 66 seeds) based on the residual errors computed by the FTRAC software. The $\sigma = 5 \text{ pixels} = 2.5 \text{ mm}$ and the threshold = 0.98 for localizing the candidate seeds were used. Since the exact locations of the seeds were unknown, the correspondence between the projection of the estimated seeds and the actual seeds in the images was visually assessed. The estimated seed locations were also compared with those computed by an existing software, MARSHAL [7] and the differences were computed. In Figure 2 are shown an example patient image and a magnified image onto which the centroids of the estimated seeds are projected. All seeds were well matched for both cases and the results are shown in Table 3.

4. CONCLUSIONS

A novel method for prostate brachytherapy seed reconstruction using C-arm images was described. Modified distance map images are generated from 2-D projection images and are used for tomosynthesis-based 3-D reconstruction. True seed locations are

Table 1. Simulation results using different number of images for different data sets.

Number of true seeds	72		96		112	
Number of images used	3	4	3	4	3	4
Number of candidate seeds	73.6	72.0	104.9	97.1	121.7	113.9
Correctly estimated seeds (%)	100	100	98.3	100	98.9	99.6
Mean reconstruction error (mm)	0.61	0.57	0.64	0.58	0.65	0.57
STD of reconstruction errors (mm)	0.14	0.09	0.31	0.11	0.24	0.11

Table 2. Phantom experiment results using different number of images for different data sets.

Number of true seeds	42			72			102		
Number of images used	4	5	6	4	5	6	4	5	6
Number of candidate seeds	43	42	42	75	72	72	117	112	107
Correctly estimated seeds (%)	100	100	100	98.6	100	100	93.1	97.1	97.1
Mean reconstruction error (mm)	1.75	1.26	1.05	1.04	0.67	0.65	1.27	1.50	0.98
STD of reconstruction errors (mm)	0.64	0.52	0.42	0.44	0.41	0.37	0.55	0.46	0.50

Table 3. Clinical experiment results.

Number of true seeds	61	66
Number of images used	3	3
Number of candidate seeds	68	80
Correctly matched seeds (%)	100	100
Mean reconstruction difference (mm)	0.96	1.04
STD of reconstruction difference (mm)	0.61	0.72

separated from a set of candidate seeds detected from the reconstruction by solving optimal coverage problem. This method requires slightly larger number of images compared to the 2-D image-based approach, but the attractive feature of the proposed method is that it can recover all the seeds automatically, including the hidden seeds, without an exact seed identification. Through simulations, phantom, and clinical studies, our method was evaluated, successfully localizing the implanted seeds. Further validation on more clinical data will be shown in a future publication.

Acknowledgements: We thank Dr. Danny Y. Song and Anton Deguet for acquiring the patient data and technical support.

5. REFERENCES

- [1] A. Jemal, R. Siegel, E. Ward, T. Murray, J. Xu, and M. J. Thun, "Cancer statistics," *CA Cancer J. Clin.*, vol. 57, pp. 43–66, 2007.
- [2] M. D. Altschuler and A. Kassaei, "Automated matching of corresponding seed images of three simulator radiographs to allow 3D triangulation of implanted seeds," *Phys. Med. Biol.*, vol. 42, pp. 293–302, 1997.
- [3] D. Tubic, A. Zaccarin, L. Beaulieu, and J. Pouliot, "Automated seed detection and three-dimensional reconstruction, ii. reconstruction of permanent prostate implants using simulated annealing," *Med. Phys.*, vol. 28, pp. 2272–2279, 2001.
- [4] S. Narayann, P. Cho, and R. Marks, "Fast cross-projection algorithm for reconstruction of seeds in prostate brachytherapy," *Med. Phys.*, vol. 29, pp. 1572–1579, 2002.
- [5] D. A. Todor, G. N. Cohen, H. I. Amols, and M. Zaider, "Operator-free, film-based 3d seed reconstruction in brachytherapy," *Phys. Med. Biol.*, vol. 47, no. 12, pp. 2031–2048, 2002.
- [6] S. T Lam, P. S. Cho, R. J. MarksII, and S. Narayanan, "Three-dimensional seed reconstruction for prostate brachytherapy using hough trajectories," *Phys. Med. Biol.*, vol. 49, no. 4, pp. 557–569, 2004.
- [7] A. K. Jain, Y. Zhou, T. Mustafa, E. C. Burdette, G. S. Chirikjian, and G. Fichtinger, "Matching and reconstructoin of brachytherapy seeds using the hungarian algorithm (MARSHAL)," *Med. Phys.*, vol. 32, pp. 3475–3492, 2005.
- [8] Y. Su, B. J. Davis, M. G. Herman, and R. A. Robb, "Prostate brachytherapy seed localization by analysis of multiple projections: Identifying and addressing the seed overlap problem," *Med. Phys.*, vol. 31, pp. 1277–1287, 2004.
- [9] V. Singh, L. Mukherjee, J. Xu, K. R. Hoffmann, P. M. Dinu, and M. Podgorsak, "Brachytherapy seed localization using geometric and linear programming technique," *IEEE Trans. Med. Imag.*, vol. 26, pp. 1291–1304, 2007.
- [10] C. Labat, A. K. Jain, G. Fichtinger, and J. L. Prince, "Toward optimal matching for 3D reconstruction of brachytherapy seeds," *LNCS*, vol. 4792, pp. 701–709, 2007.
- [11] I. B. Tutar, R. Managuli, V. Shamdasani, P. S. Cho, S. D. Pathak, and Y. Kim, "Tomosynthesis-based localization of radioactive seeds in prostate brachytherapy," *Med. Phys.*, vol. 30, pp. 101–109, 2003.
- [12] X. Liu, A. K. Jain, and G. Fichtinger, "Prostate implant reconstruction with discrete tomography," *LNCS*, vol. 4791, pp. 734–742, 2007.
- [13] A. K. Jain, T. Mustafa, Y. Zhou, C. Burdette, G. S. Chirikjian, and G. Fichtinger, "Frac - a robust fluoroscope tracking fiducial," *Med. Phys.*, vol. 32, pp. 3185–3198, 2005.
- [14] Y. Su, D. J. Davis, M. G. Herman, A. Manduca, and R. A. Robb, "Examination of dosimetry accuracy as a function of seed detection rate in permanent prostate brachytherapy," *Med. Phys.*, vol. 32, pp. 3049–3056, 2005.

Dynamic Dosimetry and Edema Detection in Prostate Brachytherapy - a Complete System

A. Jain¹, A. Deguet¹, I. Iordachita¹, G. Chintalapani¹, J. Blevins³, Y. Le², E. Armour², C. Burdette³, D. Song², G. Fichtinger⁴

1 - Johns Hopkins University; 2 - Johns Hopkins School of medicine; 3 - Acoustic MedSystems Inc.; 4 - Queen's University

ABSTRACT

Purpose: Brachytherapy (radioactive seed insertion) has emerged as one of the most effective treatment options for patients with prostate cancer, with the added benefit of a convenient outpatient procedure. The main limitation in contemporary brachytherapy is faulty seed placement, predominantly due to the presence of intra-operative edema (tissue expansion). Though currently not available, the capability to intra-operatively monitor the seed distribution, can make a significant improvement in cancer control. We present such a system here.

Methods: Intra-operative measurement of edema in prostate brachytherapy requires localization of inserted radioactive seeds relative to the prostate. Seeds were reconstructed using a typical non-isocentric C-arm, and exported to a commercial brachytherapy delivery system. Technical obstacles for 3D reconstruction on a non-isocentric C-arm include pose-dependent C-arm calibration; distortion correction; pose estimation of C-arm images; seed reconstruction; and C-arm to TRUS registration.

Results: In precision-machined hard phantoms with 40-100 seeds and soft tissue phantoms with 45-87 seeds, we correctly reconstructed the seed implant shape with an average 3D precision of 0.35 mm and 0.24 mm, respectively. In a DoD Phase-1 clinical trial on 6 patients with 48-82 planned seeds, we achieved intra-operative monitoring of seed distribution and dosimetry, correcting for dose inhomogeneities by inserting an average of 4.17 (1-9) additional seeds. Additionally, in each patient, the system automatically detected intra-operative seed migration induced due to edema (mean 3.84 mm, STD 2.13 mm, Max 16.19 mm).

Conclusions: The proposed system is the first of a kind that makes intra-operative detection of edema (and subsequent re-optimization) possible on any typical non-isocentric C-arm, at negligible additional cost to the existing clinical installation. It achieves a significantly more homogeneous seed distribution, and has the potential to affect a paradigm shift in clinical practice. Large scale studies and commercialization are currently underway.

Keywords: Fluoroscopic guidance, Prostate brachytherapy, Low cost, Edema.

1. INTRODUCTION

With an annual incidence of over 200,000 new cases & 33,000 deaths in the US, prostate cancer continues to be the most common cancer in men,¹ and is expected to double its incidence rates by 2015. Currently one in every six men get diagnosed with it at some point in their life. For several decades, the definitive treatment for low risk prostate cancer was radical prostatectomy or external beam radiation therapy (EBRT). However, developments in prostate brachytherapy have seen it emerge as a primary treatment option, with recent studies showing an overall 15-year survival rate of 74% (88%, 80% & 53% in low, intermediate & high-risk patients). Improved patient selection and implant quality has resulted in multiple brachytherapy reports demonstrating survival rates equivalent to the best published radical prostatectomy and EBRT outcomes.² This has lead to a large increase in the number of brachytherapy procedures, with 30%-40% of all prostate cancer patients receiving brachytherapy as part of their treatment,³ while utilization rates for prostatectomy and external-beam radiotherapy have fallen by over 10%. It is currently estimated that at over 50,000 brachytherapy procedures are performed annually.

Brachytherapy is a convenient one-time outpatient procedure, without the surgical trauma of prostatectomy or the grinding routine of EBRT. In this treatment a number of small ($\sim 1 \times 5$ mm) radioactive capsules are implanted into the prostate to kill the cancer by emitting radiation. It was first performed in 1911 with limited

success. In the 1960's, the use of Au-198 & I-125 isotopes triggered modern day permanent seed implantation. Many new techniques were introduced, but their limitations prevented widespread adoption. Nevertheless, it was found that disease control was better in early-stage patients who received high-quality implants (60% versus 20% local control).³ The advent of transrectal ultrasound (TRUS)-guided procedures in the 1980's, along with computerized planning, lead to an increase in seed placement accuracy and a superior distribution of the seeds throughout the prostate. Early results showed that patients treated between 1988-90, performed better than those treated by the same physicians between 1986-87, the only difference being the quality of the implant. This further supported the hypothesis that higher-quality implants resulted in better outcomes. As the procedure has become more and more popular, many technical improvements have been added (eg. inverse planning and post-op CT) to improve the implant quality.

With virtually all studies agreeing that a high quality implant is the key to successful outcomes, the next paradigm shift is expected to be the capability to intra-operatively monitor the inserted seeds. The biggest bottleneck toward this, is seed migration induced by edema. This causes insufficient dose to the cancer and/or excess radiation to the rectum, urethra, and bladder. Edema is a natural response of the body, wherein the tissue expands due to the needle-insertions and radiation. Studies have shown that edema could increase the prostate volume by up to 100%, decreasing exponentially with time (mean half-life of 9.3 days), and potentially underdosing some patients by as much as 32%.⁴ A small fraction of brachytherapy patients suffer from adverse side-effects like secondary malignancies in the rectum & bladder (7.6%⁵). Minor side-effects include temporary urinary symptoms (50-80%⁶), rectal bleeding (2-5%³) and sexual impotency (20%³). All these side-effects stem from imperfect execution of the intended plan, mostly due to edema. Thus, with the emphasis shifting to quality of life after treatment, intra-operative monitoring of seed distribution has become the holy grail.

In order to avoid over/under-dosing, the seed locations need to be determined intra-operatively, which is difficult, owing to significant seed migration due to edema. Contemporary research has tried to monitor the seeds from TRUS images by linking seeds with spacers,⁷ using X-rays to initialize segmentation,⁸ using vibro-acoustography,⁹ transurethral ultrasound¹⁰ as a new imaging modality, or segmenting them directly in TRUS images,¹¹ sometimes by using specially manufactured corrugated seeds that are better visible than conventional ones.¹² But even when meticulously hand-segmented, up to 25% of the seeds remain hidden in TRUS.¹³ The seeds have excellent visibility under X-rays, with C-arms being ubiquitous (60% availability) in brachytherapy for gross visual assessment.¹⁴ In spite of significant efforts that have been made towards computational fluoroscopic guidance in general surgery,¹⁵ C-arms cannot yet be used for intra-operative brachytherapy guidance due to a plethora of technical limitations. While several groups have published protocols and clinical outcomes favorably supporting C-arm fluoroscopy for intra-operative dosimetric analysis,¹⁶⁻¹⁸ this technique is yet to become a standard of care across hospitals. The most important current limitation towards a standard of care system, is the inability to use a non-isocentric C-arm, the type most commonly found in hospitals.

To achieve intra-operative monitoring in prostate brachytherapy, we report a new system that reconstructs 3D seed locations (visible in X-ray) and spatially registers them to the prostate (visible in TRUS). We discuss briefly the variety of technical issues in Section 2, following up with results from phantom experiments & a Phase-I clinical trials in Section 3. Our primary contribution to the state of the art is our ability to use any typical non-isocentric uncalibrated C-arm present in most hospitals. We believe that the availability of this technology, followed up with large scale clinical studies and commercialization (ongoing), promises to lead to a paradigm shift in the standard of care for image-guided prostate brachytherapy.

2. METHODS AND MATERIALS

The system is designed to easily integrate easily with commercial brachytherapy installations. We employ a regular clinical brachytherapy setup, without alteration, including a treatment planning workstation & stabilizer/stepper (Interplant®, CMS, St Louis), TRUS (B&K Medical Pro Focus) and a C-arm (GE OEC 9600/9800). The C-arm is interfaced with a laptop through an NTSC video line and frame grabber, making the image capture independent of the C-arm model.

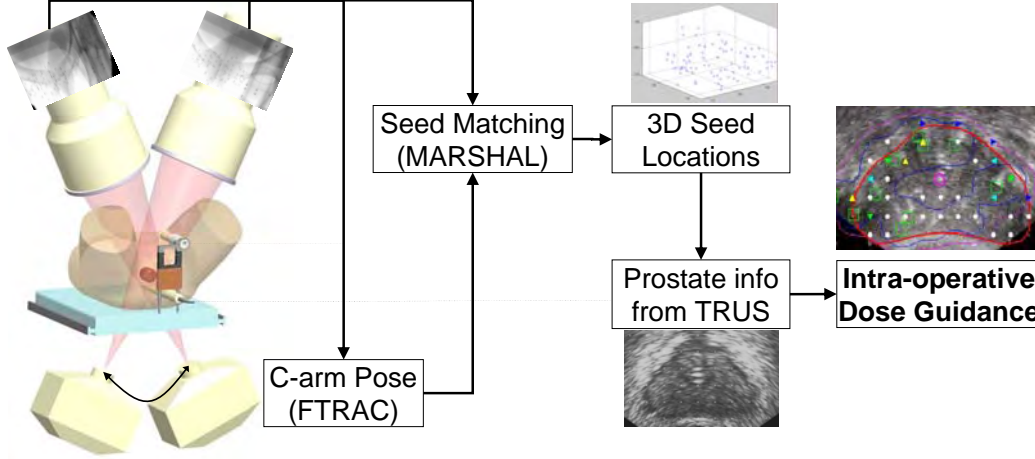


Figure 1. Overview of the proposed solution. The FTRAC fiducial tracks C-arms, and also registers TRUS to C-arm images, making quantitative brachytherapy possible.

Workflow: The clinical workflow (Fig. 1) is identical to the standard procedure until the clinician decides to run a reconstruction and optimization. A set of C-arm images are collected with *a separation as wide as clinically possible* (usually 10° around AP-axis) and synchronously transferred to the laptop. After processing the images, the seeds are reconstructed and their 3D locations exported to the Interplant[®] system. The physician uses standard Interplant[®] tools to analyze, optimize and modify the remainder of the plan. The procedure concludes when the exit dosimetry shows no cold spots (under-radiated locations).

Numerous technical obstacles have to be overcome to realize C-arm based intra-operative dosimetry: (a) pose estimation of C-arm images; (b) C-arm calibration; (c) image distortion correction; (d) seed segmentation; (e) seed matching & reconstruction; (f) registration of C-arm to TRUS; (g) dosimetry analysis; and finally (h) implant optimization. We have developed a system that overcomes these limitations in providing quantitative intra-operative dosimetry. In what follows, we will describe briefly each component of the system, skipping the detailed mathematical framework.

Pose Estimation: The most critical component of a clinically usable solution for 3D fluoroscopic guidance is C-arm pose estimation. C-arms available in most hospitals do not have encoded rotational joints, making the amount of C-arm motion unavailable. C-arm tracking using auxiliary trackers is expensive, inaccurate in the presence of metal (EM tracking) or intrudes in the operating room (optical tracking). There has been some prior work on fiducial based tracking, wherein a fiducial is introduced in the X-ray FOV and its projection in the image encodes the 6 DOF pose of the C-arm. The most significant problem in contemporary designs is that though sufficiently accurate, they are too bulky to be easily used in a clinical setting. To improve clinical usability, the size of the fiducial can be decreased, usually at a significant expense of the accuracy.

We proposed a new fluoroscope tracking fiducial design, FTRAC, that uses an ellipse.¹⁹ The fiducial is illustrated in Figure 2, 5. The ellipse makes pose recovery accurate by (a) always projecting as an ellipse; (b) allowing an accurate segmentation; and (c) providing closed form Jacobian formulations for fast optimization. The FTRAC design has salient features, including small dimensions (3x3x5cm), no special proximity requirements to the anatomy, and is relatively inexpensive. In particular, the small size makes it easier to be always in the FOV & to be robust to image distortion. Extensive phantom experiments indicated a mean tracking accuracy on distorted C-arms of 0.56 mm in translation and 0.19° in rotation, an accuracy comparable to expensive external trackers.

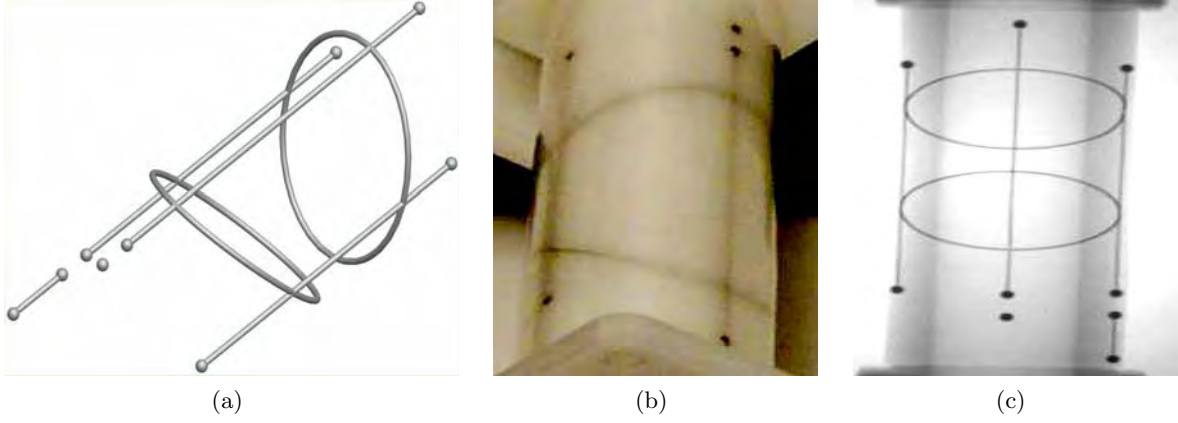


Figure 2. Images of the FTRAC fiducial (a) wire model; (b) photograph; (c) X-ray image

C-arm Source Calibration and Image Distortion: Since both C-arm calibration and distortion are pose-dependent, contemporary fluoroscopy guidance systems calibrate/ distortion-correct at each imaging pose. This is done using a cumbersome calibration-fixture, which is a significant liability. Our approach is a complete departure. Using a mathematical & experimental framework, we demonstrated that calibration is not critical for prostate seed reconstruction; *i.e.* just an approximate pre-operative calibration suffices. The central intuition is that object reconstruction using a mis-calibrated C-arm changes only the absolute positions of the objects, but not their relative ones (Fig. 3). Additionally, statistical analysis of the distortion on a GE OEC 9600, inside a 15° limited workspace revealed that just a single pre-operative correction at the AP-axis can reduce the average distortion in the image from 3.31 mm to 0.51 mm. These errors are expected to be similar for most modern C-arms, with a more involved discussion available in.²⁰ This residual amount of distortion in the X-ray image is acceptable for accurate 3D reconstruction, especially when used with image based C-arm tracking.

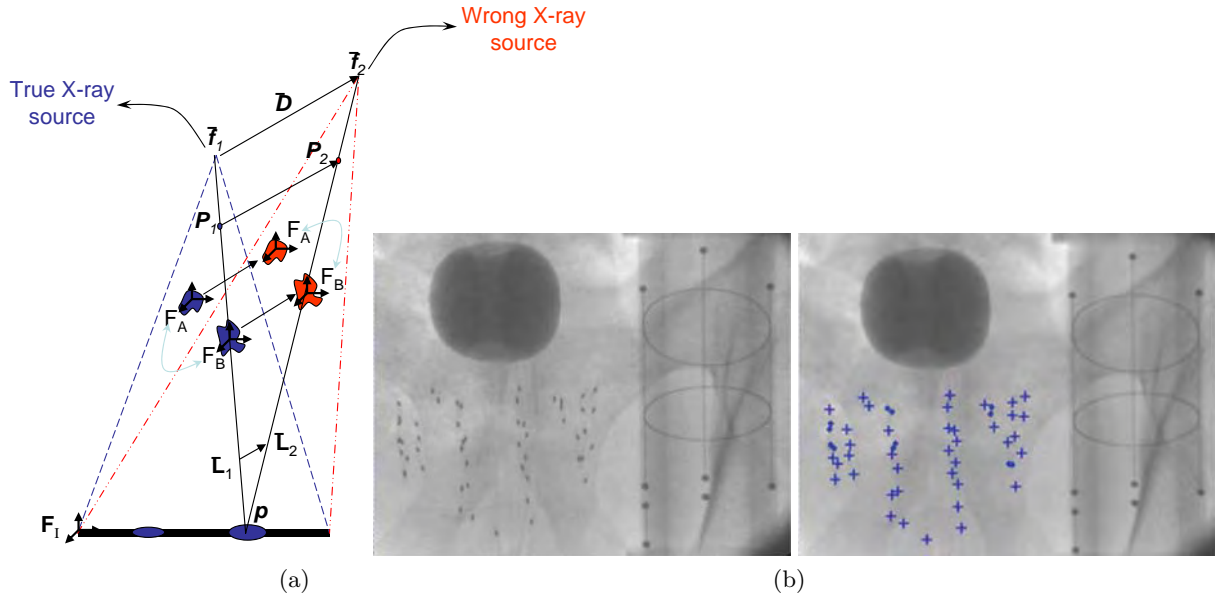


Figure 3. (a) Mis-calibration conserves relative reconstruction between objects A and B (eg. seeds). (b) X-ray image before segmentation (left). There is also the FTRAC in the image. The image after segmentation (right); the blue '+' symbol represent individual seeds and the blue '.' indicates a seed that is a part of a multiple seed cluster.

Seed Segmentation: Seed segmentation in C-arm video images is usually hindered by poor image resolution. We developed an automated seed segmentation algorithm that employs the morphological top-hat transform to perform the basic seed segmentation, followed by thresholding, region labeling, and finally a statistical classification into two classes - single seeds and clusters containing overlapping seeds. Using some simple ellipse partitioning techniques, these clustered seeds are finally broken down into single seeds. The algorithm was tested on clinical images and found to be sufficiently accurate. Out of total 763 seeds from 10 patient images of Palladium implants, 758 seeds were correctly identified; only 2 seeds clusters were not correctly resolved and 2 false positives were added. The segmentation is verified on the screen to allow for a manual bypass by the surgeon.

Seed Correspondence & Reconstruction: The 3D coordinates of the implanted seeds can now be triangulated by resolving the correspondence of seeds in the multiple X-ray images. As explained in²¹ we formalized the seed correspondence as a combinatorial optimization problem. As seen in Figure 4, a network is created where any flow represents a matching, the desired solution being the flow with minimum cost, computed using the cycle-canceling algorithm. Our formulation has many preferred features: (a) exact solutions; (b) claims on the problem complexity; and (c) optimality considerations. We showed that a polynomial-time perfect solution is not achievable and proposed a practical solution (MARSHAL) that runs practically in $O(N^3)$ using any number of images, where N is the number of inserted seeds. In comparison, previous solutions have predominantly been heuristic explorations of the large search space. In addition, the framework robustly resolves all the seeds that are hidden in the images (as many as 7% can be hidden due to the high seed density). A simple extension to the network at strategic nodes, allowing a flow of 2 units instead of 1, enables MARSHAL to also automatically recover hidden seeds. MARSHAL typically reconstructs 99.8% of the seeds and runs in under 5s in MATLAB, exhibiting a significantly higher than the required minimum-detection-rate of 95% that has been suggested.²²

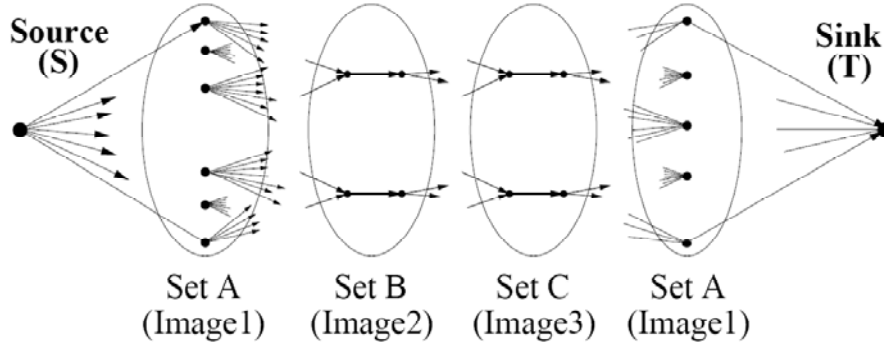


Figure 4. The network flow formulation used to solve the hidden-seed correspondence problem.

Registration of C-arm to TRUS: The 3D seed coordinates are reconstructed with respect to the FTRAC and need to be registered to the prostate boundaries visible in the TRUS images. This is a difficult problem, owing to the lack of physical access to the patient-anatomy and the inherently complementary natures of the two modalities. X-rays predominantly images hard tissue, while Ultrasound looks at soft tissue boundaries. In a quick survey of X-ray to TRUS registration, various groups have attempted to use catheters, gold marker seeds, needles or the inserted radioactive seeds as markers. Unfortunately, implanted markers in Ultrasound are very hard to differentiate from various other objects like inserted seeds & needle tracts. Moreover, they are also susceptible to intra-operative tissue expansion, making the registration unreliable. Alternately, radio-opaque beads were attached to the probe and have been used for registration, requiring a permanent alteration to the probe, which for many practitioners is not desirable. Altogether, a comprehensive and clinically reliable solution for spatial registration of fluoroscopy and TRUS images is currently not known.

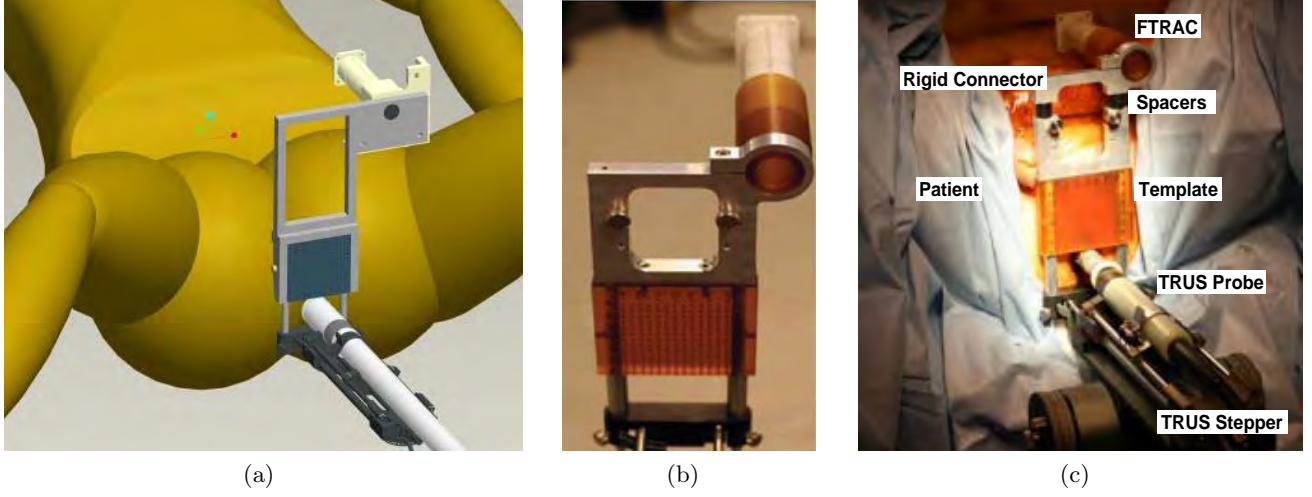


Figure 5. The FTRAC fiducial & the needle insertion template can be pre-calibrated using a rigid mount.(a) A CAD model of the FTRAC fiducial mounted on the seed-insertion needle template using a rigid connector. (b) An actual photograph of the FTRAC mounted on the template.(c) A zoomed annotated photograph of the clinical setup.

In commercial brachytherapy systems the needle insertion template is already pre-registered to TRUS probe as per the FDA approved clinical protocol. Hence, we propose to mount the FTRAC fiducial on top of this template in a known rigid position, using a precision-machined mechanical connector. The arrangement is illustrated in Figure 5. Thus a simple application of the various known frame transformations, registers the 3D seeds (FTRAC) to the prostate (TRUS).

System Implementation: We have integrated the previously discussed functions into a complete MATLAB program with a graphical user interface. Screen-captures from the program are shown in Figure 6. The package runs on an ordinary laptop that sends reconstructed seed positions to Interplant[®] system. In order to not require a new FDA approval, we maintain the integrity of the FDA-approved Interplant[®] system by not modifying the commercial software. We instead use a text file to export the 3D seed locations.

Dosimetry Analysis and Implant Optimization: The seed locations (in template coordinates) are exported to the Interplant[®] system. A software patch added to the Interplant[®] removes the already implanted seeds from the original plan, thereby producing a "*residual implant plan*". The total dose is calculated by combining the current seed locations and those in the residual implant plan. The physician at this stage, modifies the residual plan to avoid any potential 'hot spots' (prostate tissue receiving significantly more than prescribed radiation dose), and most importantly, fills in any observed cold spots (under-dosed prostate tissue receiving less than prescribed radiation). This process can be repeated any number of times during the surgery, achieving a more homogenous seed distribution.

Clinical Workflow: The procedure flows in two main branches as shown in Figure 6 (b). In addition to the FDA approved TRUS-template calibration, the pre-operative phase now also includes the C-arm calibration. Intra-operatively, the procedure proceeds without any alterations. At any point, the physician can decide to incorporate the current 3D seed locations, in which an X-ray reconstruction is carried out. The TRUS probe is retracted to prevent the transducer from blocking the C-arm's field of view. With moving the C-arm over the target area, 3-4 X-ray images are collected. Each image provides a view of the prostate (with the implanted seeds) and the FTRAC fiducial. These images are automatically captured by the computer using a framegrabber. The intra-operative workflow continues with extensive image analysis, as described so far. Each C-arm image is

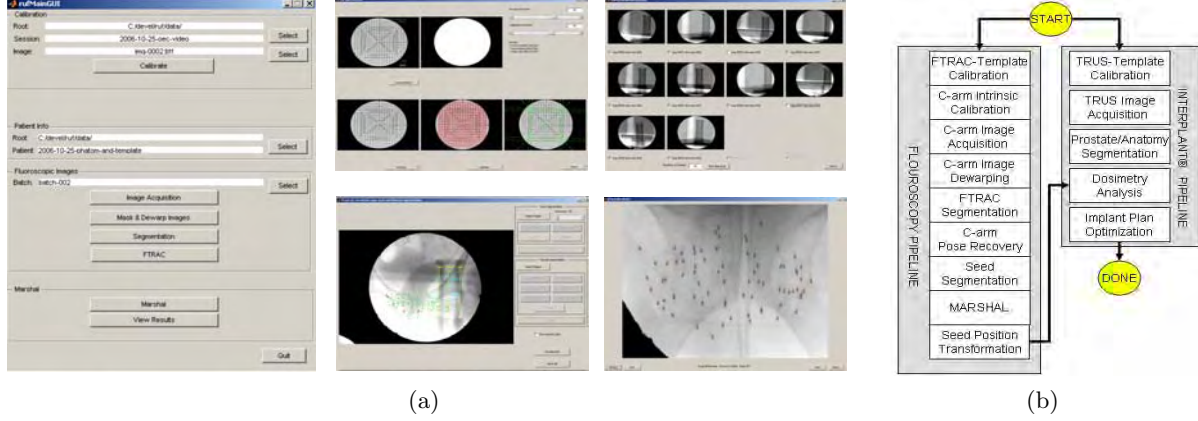


Figure 6. (a) GUI screen captures of the main program, offline calibration, seed & fiducial segmentation, seed matching and validation of the reconstruction by back-projection. (b) Workflow for intra-operative dose optimization.

automatically corrected for distortion. Next, the segmentation algorithm segments the motifs of the FTRAC fiducial and recovers the relative poses of the C-arm images, followed by the segmentation of all visible seeds in the images. MARSHAL then matches all the segmented seeds and reconstructs their 3D locations, while also recovering the seeds hidden in one or more images. Finally, we apply the predetermined coordinate transformation to the seed cloud to obtain the position of the seeds in template coordinates and send them to the Interplant[®], where the dose coverage relative to the relevant anatomy is analyzed and the remainder of the implant plan optimized. At this point, the clinical workflow reverts back to the default standard of care protocol.

3. PHANTOM EXPERIMENTS AND RESULTS

We have extensively tested the system and its components in various phantoms and in a Phase-1 clinical trial. To do so, we introduce the terms **absolute** and **relative** reconstruction errors. Using X-ray images, the seeds are reconstructed with respect to the FTRAC frame. In experiments where the ground truth location of the seeds with respect to the FTRAC is known, the comparative analysis of the seed locations is called **absolute** accuracy. Sometimes (eg. in patients), the true seed locations with respect to the FTRAC are not available and the reconstruction can only be compared to the seeds extracted from post-operative data (using a rigid point-cloud to point-cloud transform), in which case the evaluation is called **relative** accuracy.

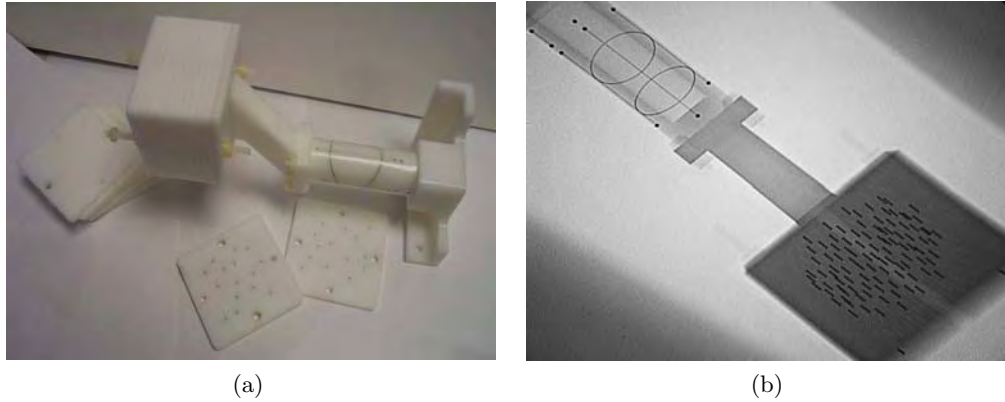


Figure 7. (a) An image of the seed phantom attached to the FTRAC fiducial. The phantom can replicate any implant configuration, using the twelve 5 mm slabs each with over a hundred holes. (b) A typical X-ray image of the combination.

Solid Seed Phantom: An acetol (Delrin) phantom consisting of ten slabs (5mm each) was fabricated (Figure 7). This phantom provides a multitude of implants with sub-mm ground truth accuracy. The fiducial was *rigidly* attached to the phantom in a known way, establishing the accurate ground truth 3D location of each seed. Realistic prostate implants (1.56 seeds/cc, 40-100 seeds) were imaged within a 30° cone around the AP-axis. The true correspondence was manually established by using the 3D locations, known from the precise fabrication. Averaged results indicate that we correctly match 98.5% & 99.8% of the seeds using 3 & 4 images (100 & 75 total trials) respectively. The mean 3D absolute reconstruction accuracy was 0.66 mm (STD 0.29 mm), while the relative accuracy was 0.35 mm. Furthermore, using 4 images yielded only one poorly mis-matched seed from the 75 datasets, suggesting the use of 4 images for better clinical guidance.

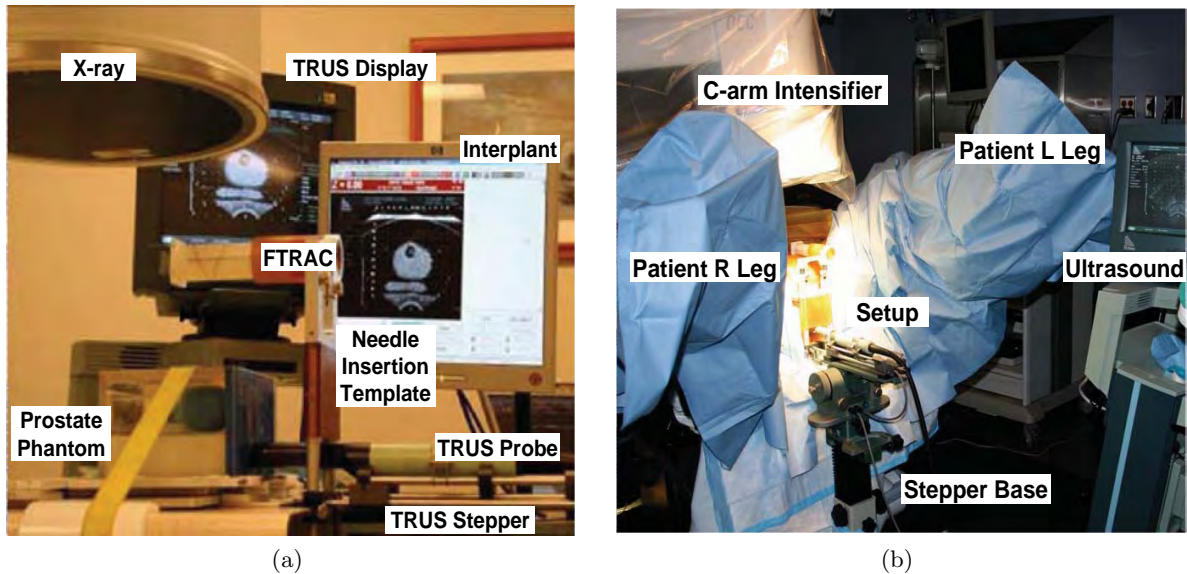


Figure 8. An annotated image of the (a) experimental setup for the training phantom experiments; (b) overall set up of the full operating area during the Phase-I clinical trials.

Soft Training Phantoms: As annotated in Figure 8, we fully seeded three standard prostate brachytherapy phantoms with realistic implant plans (45, 49, 87 seeds). Seed locations reconstructed from fluoro using realistic (maximum available clinically) image separation (about 15°) were compared to their corresponding ground truth locations segmented manually in CT (1mm slice thickness). Additionally, the 45 & 87-seed phantoms were rigidly attached to the FTRAC, providing the absolute ground truth (from CT). The 49-seed phantom was used to conduct a full scale practice-surgery, in which case the 3D reconstruction could be compared only to the seed cloud from post-op CT (without FTRAC), providing just relative accuracy.

The performance of the system on the soft tissue training phantoms is tabulated in Table 1. The absolute reconstruction errors for the 45, 87-seed phantoms were 1.64 mm & 0.95 mm (STD 0.17 mm), while the relative reconstruction errors for the 45, 49, 87-seed phantoms were 0.22 mm, 0.29 mm, 0.20 mm (STD 0.13 mm). A mean translation shift of 1.32 mm was observed in the 3D reconstructions, predominantly due to the limited C-arm workspace (solid-phantom experiments with 30° motion have 0.65 mm accuracy). It was observed that the shift was mostly random & not in any particular direction. In fact, it was noticed that if different combinations of the X-ray images were used, it would result in different directions for the overall shift. This suggests that the shift is most probably due to the small amounts of error (sub-mm, sub-degree) in the pose estimation part of the system. Note that *our reconstruction accuracy is better than the CT resolution* (as evident from the solid seed phantom experiments). Moreover, the 3D error is larger in the Z-direction, which corresponds to the direction

Number of Seeds	Error Type	Error (mm)			3D Error (mm)	Translation Offset (mm)
		X	Y	Z		
45	Absolute	0.38	0.94	1.27	1.64	1.50
87		0.41	0.40	0.71	0.95	1.13
	Average	<i>0.40</i>	<i>0.67</i>	<i>0.99</i>	<i>1.30</i>	<i>1.32</i>
45	Relative	0.08	0.14	0.12	0.22	-
49		0.09	0.11	0.10	0.29	-
87		0.12	0.18	0.12	0.20	-
	Average	<i>0.10</i>	<i>0.14</i>	<i>0.11</i>	<i>0.24</i>	-

Table 1. Tabulated performance of the system on soft tissue training phantoms. Note the difference between the absolute and relative reconstruction errors.

of the 1 mm axial slices of the CT. Nevertheless, the accuracy is sufficient for brachytherapy, especially since a small shift does not hamper the ability to detect the presence of any cold spots.

Patients: A total of 18 batches of reconstructions were carried out on 6 patients with 2 – 4 batches/patient, as and when a need for dose evaluation was felt by the clinician. The number of seeds in each batch varied from 22 – 84. Since the seeds migrate significantly by the time a post-operative CT is taken, there is no easy method for knowing the true 3D seed locations (ground truth) in real patients. Hence, for each reconstruction 4 – 6 additional X-ray images were taken. The intra-operatively reconstructed 3D seed locations were projected on these additional images and compared to their corresponding segmented 2D locations (post-operatively). The results from a total of 99 such projections from 18 reconstructions are tabulated in Table 2.

Patient Number	Number of Seeds	Additional X-ray Images	Error in X-ray Image (mm)			
			Mean	STD	Max	Min
1	22	6	2.32	0.21	2.75	1.92
	44	5	2.24	0.31	2.86	1.47
	65	5	1.19	0.29	1.95	0.52
	66	5	1.01	0.23	1.70	0.53
2	39	5	1.20	0.21	1.67	0.81
	84	4	2.16	0.60	4.18	0.35
3	33	5	1.19	0.27	1.88	0.63
	67	6	1.60	0.44	2.76	0.74
	70	4	1.47	0.64	3.22	0.38
4	35	5	1.21	0.21	1.64	0.75
	68	6	1.43	0.42	3.05	0.41
	77	5	1.81	0.29	2.59	1.15
5	24	6	2.30	0.45	3.09	1.46
	48	6	2.19	0.46	3.51	1.07
	53	7	2.17	0.41	3.40	1.51
6	33	6	1.90	0.32	2.67	1.34
	61	7	2.30	0.34	3.44	1.49
	66	6	1.40	0.29	2.14	0.76
Average	56	5.5	1.57	0.34	2.50	0.83

Table 2. 18 intra-operative 3D X-ray seed reconstructions with 22-84 seeds, projected back on additional 99 (unused) X-ray images. Note that the maximum error is never remarkably huge.

The results indicate a 2D mean error of 1.57 mm (STD 0.34 mm , max 2.50 mm , min 0.83 mm). This indicates a sub-mm accuracy in 3D reconstruction, since the errors get magnified under a perspective transform when projected from 3D to a 2D image. Though the magnification factor varies for each image depending on the relative depth of the seeds with respect to the C-arm focal length, it ranges approximately from $1.5 - 2$. This indicates an average absolute 3D reconstruction accuracy of $0.8 - 1.0\text{ mm}$, which is similar to the results obtained from the phantom experiments. Further note that the average minimum error is 0.83 mm , indicating that there is a small consistent *shift/bias* in the reconstruction. This collaborates completely with the observations that were made earlier. In only one case (patient-2 84-seeds), we see a maximum error more than 4 mm . However, in these cases we also observe that the overall deviation is higher too, indicating that these datasets might have a larger 3D *shift/bias*. In any case, we do not see the maximum error go many deviations away from the mean error. A 2.5 mm error in 3D is expected to project as a 5 mm error at least in some of the X-ray images, which we have not observed. This indicates that we had successful intra-operative reconstructions in the Phase-I patient trials.

Registration Accuracy: To measure the accuracy of the fiducial-to-template registration, three batches of five straight needles each were inserted randomly at known depths (Z-axis) into known template holes (X, Y-axis). Their reconstructed tip locations with respect to the FTRAC coordinate-frame were transformed to the template coordinate-frame using our rigid registration transform, which were then compared to their true measured locations in template coordinates. The limited-angle image-capture protocol was kept similar to that used in the operating room. Both absolute and relative results are tabulated in Table 3. The average absolute error (reconstruction together with registration) was 1.03 mm (STD 0.18 mm), while the average relative error was 0.36 mm (STD 0.21 mm), with an average translation shift of 0.97 mm . Note that the performance of the system in these experiments is similar to the performance of the system in the other experiments presented so far, strengthening the validity of our conclusions.

Trial Number	Error Type	Error (mm)			3D Error (mm)	Translation Offset (mm)
		X	Y	Z		
1	Absolute	0.32	0.70	0.84	<i>1.16</i>	1.15
2		0.66	0.29	1.02	<i>1.27</i>	1.22
3		0.12	0.28	0.54	<i>0.65</i>	0.55
1	Relative	0.11	0.17	0.05	<i>0.22</i>	-
2		0.10	0.27	0.35	<i>0.49</i>	-
3		0.10	0.27	0.19	<i>0.36</i>	-

Table 3. 3 sets of 5 needles were inserted into the template at known depths and reconstructed. This comparison gives us the cumulative 3D error from X-ray reconstruction with respect to FTRAC and FTRAC-template registration, *i.e.* 3D reconstruction error with respect to the template.

System Accuracy: To measure the full system error, 5 needles (tips) were inserted into a prostate brachytherapy training phantom, reconstructed in 3D and exported to the Interplant[®] software. The needle tips were also segmented manually using TRUS images. The sagittal images were used for measuring the depth (Z-axis) of the needles and the transverse images were used to measure the planar positions (X,Y-axis), providing ground truth from Ultrasound. The mean absolute error for the 5 needle tips was 4 mm (STD 0.53 mm), with a translation shift of 3.94 mm . In comparison, the relative accuracy for the complete system was 0.83 mm (STD 0.18 mm).

The shift can mainly be attributed to (i) an error in the Template-TRUS pre-calibration done as part of current clinical practice, resulting in a shift ($\sim 3\text{ mm}$); and (ii) a random bias in the 3D reconstruction due to limited image separation ($\sim 1\text{ mm}$). Nevertheless, we removed this shift in the clinical cases by applying a translation-offset to the reconstructed X-ray seed coordinates. Owing to the small size of the prostate, the

rotation offset was always found to be minimal and could be ignored. The resultant translation offset was intra-operatively estimated by comparing the centroid of the reconstructed seeds with that of the planned seed locations, and by aligning the two together. Note that the centroid is a first-order statistic and robust to any spatially symmetric noise/displacement model. Though a heuristic, it provided excellent qualitative results according to the surgeon, who read the visual cues at the reconstructed seed locations in TRUS images. Based on the experiments so far and the surgeon's feedback, the overall accuracy of the system is expected to be $1 - 2\text{ mm}$ during clinical use.

Phase-I Clinical Trial: We have treated a cohort of 6 patients, as part of a DoD Phase-I clinical trial to test the efficacy and safety of the system (the Phase-II trial is currently open for enrollment). Annotated photographs of the clinical setup are shown in Figure 5 (c) & 8 (b). Intra-operative dosimetry was performed (i) halfway during the surgery; (ii) at the end of the surgery; and (iii) after all the additional seeds were inserted. The current protocol adds about 15 minutes for each reconstruction, including the capture of 5 extra X-ray images for research validation, image processing, 3D seed reconstruction, and dosimetry optimization. In regular everyday clinical practice, we anticipate the need for only a single exit-dosimetry reconstruction, increasing the operating time only by about 10 minutes. *In all the patients the final dosimetry detected cold spots* (Figure 9). The clinician grew quickly to trust the system in detecting cold spots, and instead minimized potential hot spots during the surgery. The medical team found the intra-operative visualization of under-dosed regions valuable, inserting an additional 4.17 seeds on an average to make the 100% prescribed iso-dose contour cover the prostate. All patients were released from the operating room with satisfactory outcomes.

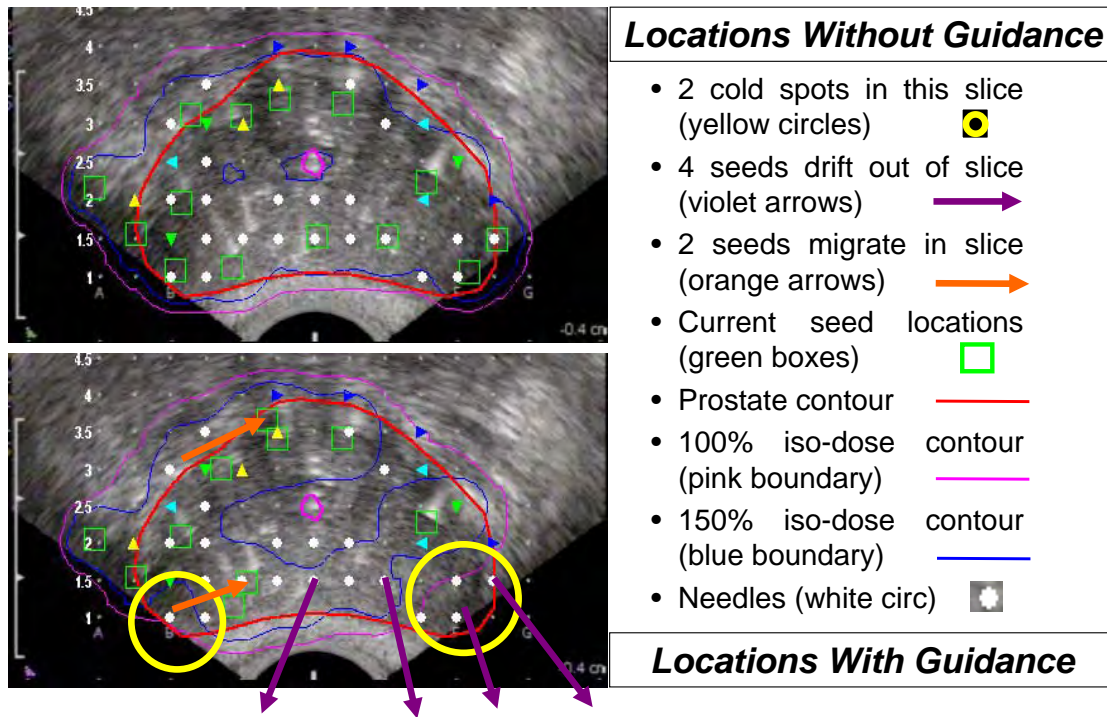


Figure 9. The system is able to detect cold spots. The seed locations (and corresponding 100/150% iso-dose contours) as **assumed** by the planning system (top) and as **computed** by the proposed system (bottom), discovering 2 cold spots in this slice. 4 seeds have drifted out of the slice, while 2 have migrated significantly within.

The *intra-operative detection and visualization of edema* was also made possible by the proposed system, as shown in Figure 10. Edema is the swelling of the prostate tissue due to the repeated stress from the punctures

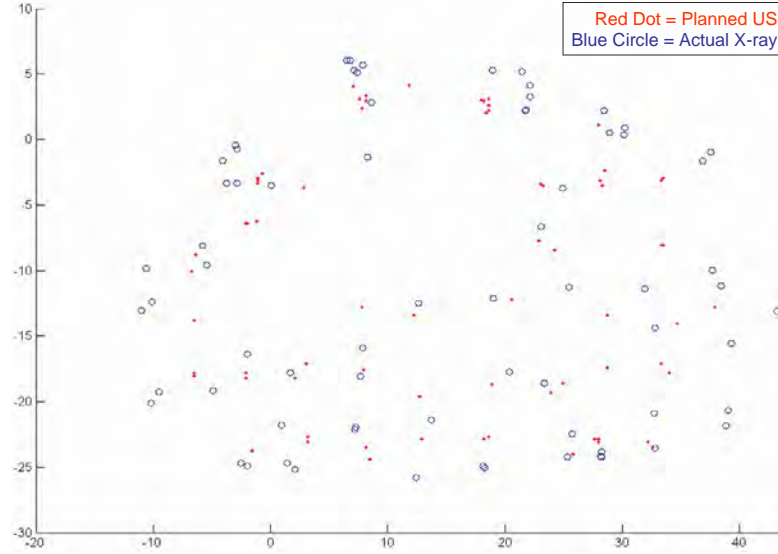


Figure 10. The system can visualize intra-operative edema, as seen for patient 3 (mean 4.6 mm, STD 2.4 mm, max 12.3 mm). The 'planned' (red) versus the 'reconstructed' (blue) seed positions as seen in the template view. A trend of outward dispersion from their initial locations is observed.

created by needle insertions and the high radioactivity from the dropped seeds. It is the single-most important source of bottleneck towards accurate dose delivery, arguably leaving behind cold spots. The system is unique, in that it is the first of a kind that can intra-operatively quantify the edema related seed migration. The system computed significant intra-operative edema in all the patients, with an average tissue expansion of 3.84 mm (STD 2.13 mm). *The seeds (and hence the prostate) showed a clear tendency for outward migration from their drop positions (with maximums up to 16 mm).* In all the patients, towards the end of the surgery, it was found that the apex of the prostate (surgeon-end) was under-dosed.

Comparison Type	Error (mm)			Norm (mm)		
	X	Y	Z	Mean	STD	Max
Pre-op TRUS to Day-0 Post-op CT (6 patients)	1.93	2.30	2.28	4.39	2.60	14.25
Pre-op TRUS to Day-30 Post-op CT (6 patients)	2.07	2.19	2.55	4.56	2.78	17.47
Day-0 Post-op CT to Day-30 Post-op CT (6 patients)	1.62	2.00	1.93	3.78	2.72	17.31

Table 4. The pre-operative planned 3D seed coordinates (TRUS) were compared to their corresponding post-operative locations computed from CT volumes. Significant seed migration due to edema can be observed.

A further comparison of the 3D final implant reconstructed using the X-ray images to Day-0 CT (2 mm slices) indicated an increased average post-operative edema of 4.39 mm (STD 2.60 mm), indicating a further post-operative seed migration in a few hours after the patient leaves the operating room. However, post-operative seed migration is an inherent limitation of brachytherapy, the best solution being a calculated intra-operative over-dosing of the patient. This makes the detection of any intra-operative edema even more critical. Brachytherapists have been traditionally accommodating for it by over-dosing the patient. Though effective, it involves some skilled qualitative guesswork on behalf of the surgeon, potentially limiting cancer control in difficult cases. Note that, in such a scenario, a sub-mm accuracy in the placement of the seeds inside the prostate could have a lesser impact on long-term cancer control.

Patient Number	Comparison Type	Error (mm)			Norm (mm)			Additional Seeds Added
		X	Y	Z	Mean	STD	Max	
1	Intra-op X-ray to Pre-op TRUS	0.26	0.41	0.45	0.77	1.09	9.00	1
2		1.91	1.88	3.18	4.65	2.20	12.23	2
3		2.50	2.13	2.28	4.59	2.36	12.26	3
4		1.59	1.57	2.68	4.27	2.53	16.02	9
5		1.61	2.67	3.05	4.98	2.83	16.19	5
6		1.47	2.30	1.88	3.78	1.76	9.82	5
Average		1.56	1.83	2.25	3.84	2.13	12.59	4.17

1	Intra-op X-ray to Day-0 Post-op CT	1.88	2.71	3.32	5.42	2.46	11.14	-
2		2.65	3.48	2.87	6.16	2.96	14.32	-
3		1.33	1.39	1.30	2.67	2.13	14.72	-
4		1.63	2.76	3.23	5.45	2.60	14.50	-
5		1.47	1.49	2.70	3.77	2.53	13.79	-
6		1.74	1.22	1.44	3.00	2.70	14.45	-
Average		1.78	2.37	2.47	4.41	2.56	13.82	-

1	Intra-op X-ray to Day-30 Post-op CT	2.64	3.62	2.57	5.78	2.49	12.04	-
2		3.45	3.84	2.86	6.84	3.32	21.75	-
3		2.04	2.55	2.13	4.70	1.97	11.17	-
4		1.70	2.40	1.87	4.07	2.14	12.51	-
5		2.45	3.27	2.83	5.70	3.10	21.87	-
6		0.97	1.51	1.67	2.91	2.42	12.49	-
Average		2.21	2.87	2.32	5.00	2.57	15.31	-

Table 5. The intra-operatively computed seed coordinates were compared those obtained from planned locations in TRUS and post-operative segmentations from CT. Additional seeds were added for each patient to close any detected cold spots.

4. CONCLUSION, SHORTCOMINGS AND FUTURE WORK

A system for intra-operative brachytherapy seed monitoring has been presented. In precision-machined hard phantoms with 40-100 seeds, we correctly reconstructed 99.8% seeds with a mean 3D accuracy of 0.35 *mm*. In soft tissue phantoms with 45-87 seeds & clinically realistic 15° C-arm motion, we correctly reconstructed 100% seeds with an accuracy of 0.24 *mm*. 18 intra-operative reconstructions from a phase-I clinical study also show a correct 3D reconstruction with under 1 mm error. This accuracy is more than sufficient for accurate intra-operative monitoring of the plan, since the system was able to measure the extent of intra-operative seed migration, showing that it could be as high as 16.19 mm (mean 3.84 mm). The proposed work was also successfully used in a Phase-I DoD clinical trial, showing usefulness and great potential.

The system (a) requires no significant hardware; (b) does not alter the current clinical workflow; (c) can be used with any C-arm; (d) integrates easily with any pre-existing brachytherapy installation; & (e) is economically feasible and scalable. There is some added radiation to the patient from the X-ray images, though insignificant when compared to that from the radioactive seeds. Though not critical, primary shortcomings include (a) 15 minute additional surgery time; & (b) a small translation bias. Research is currently underway to remove these limitations, and to conduct large scale clinical studies using clinical indicators. Commercialization is also currently in progress. Furthermore, the proposed system is the first of its kind that can intra-operatively detect seed migration using any non-isocentric C-arm, achieving a significantly more homogeneous distribution and avoiding radiation hot/cold-spots. All the above put together, promises to lead to a paradigm shift in the standard of care for image-guided prostate brachytherapy, considerably improving the patient quality of life.

5. ACKNOWLEDGMENTS

This work has been supported by DoD PC050170 - Prostate Cancer Research Program (2005) pre-doctoral Traineeship Award, NIH SBIR 1R43CA099374 01, NSF EEC-9731478.

REFERENCES

1. A. Jemal, R. Siegel, E. Ward, T. Murray, J. Xu, C. Smigal, and M. Thun, "Cancer statistics," *CA Cancer J Clin* **56**(2), pp. 106–30, 2006.
2. Sylvester et al, "15-year biochemical relapse free survival in clinical stage t1-t3 prostate cancer following combined external beam radiotherapy and brachytherapy; seattle experience," *IJRBOP* **67**(1), 2007.
3. P. Grimm and J. Sylvester, "Advances in brachytherapy," *Urology* **6**(4), pp. 37–48, 2004.
4. Yue et al, "The impact of edema on planning 125i and 103pd prostate implants," *Med Phys* **26**(5), pp. 763–7, 1999.
5. Liauw et al, "Second malignancies after prostate brachytherapy: Incidence of bladder and colorectal cancers in patients with 15 years of potential follow-up," *IJROBP* **66**(3), pp. 668–73, 2006.
6. Langley et al, "European collaborative group on prostate brachytherapy: Preliminary report in 1175 patients," *European Urology* **46**(5), pp. 565–70, 2004.
7. J. Xue, E. Gressen, and T. Jefferson, "Feasibility of trus-based prostate post-implant dosimetry," in *AAPM annual meeting*, p. Poster, July 2004.
8. Dumane et al, "Combined ultrasound-fluoroscopy approach to the intraoperative detection of seeds in prostate brachytherapy," in *ASTRO annual meeting, Poster*, Oct 3-7 2004.
9. F. Mitri, P. Trompette, and J. Chapelon, "Improving the use of vibro-acoustography for brachytherapy metal seed imaging: A feasibility study," *IEEE Trans on Medical Imaging* **23**, pp. 1–6, Jan 2004.
10. D. Holmes, B. Davis, C. Bruce, and R. Robb, "3d visualization, analysis, and treatment of the prostate using trans-urethral ultrasound," *Comput Med Imaging Graph* **27**(5), pp. 339–49, 2003.
11. D. French, J. Morris, M. Keyes, and S. E. Salcudean, "Real-time dosimetry for prostate brachytherapy using trus and fluoroscopy," in *MICCAI (2) 2004*, pp. 983–991, 2004.
12. A. Tornes and M. Eriksen, "A new brachytherapy seed design for improved ultrasound visualization," in *IEEE Symposium on Ultrasonics*, pp. 1278–83, Oct 2003.
13. B. Han, K. Wallner, G. Merrick, W. Butler, S. Sutlief, and J. Sylvester, "Prostate brachytherapy seed identification on post-implant trus images," *Med Phys* **30**(5), pp. 898–900, 2003.
14. B. Prestidge, J. Prete, T. Buchholz, J. Friedland, R. Stock, P. Grimm, and W. Bice, "A survey of current clinical practice of permanent prostate brachytherapy in the united states," *Int J Radiat Oncol Biol Phys* **15**;40(2), pp. 461–5, Jan 1998.
15. R. Hofstetter, M. Slomczykowski, M. Sati, and L. Nolte, "Fluoroscopy as an imaging means for computer-assisted surgical navigation," *Comput Aided Surg* **4**(2), pp. 65–76, 1999.
16. Reed et al, "Intraoperative fluoroscopic dose assessment in prostate brachytherapy patients," *Int J Radiat Oncol Biol Phys* **63**, pp. 301–7, Sep 2005.
17. D. Todor, M. Zaider, G. Cohen, M. Worman, and M. Zelefsky, "Intraoperative dynamic dosimetry for prostate implants," *Phys Med Biol* **48**(9), pp. 1153–71, May 7 2003.
18. French et al, "Computing intraoperative dosimetry for prostate brachytherapy using trus and fluoroscopy," *Acad. Rad.* **12**, pp. 1262–72, Oct 2005.
19. A. Jain, T. Mustufa, Y. Zhou, E. C. Burdette, G. Chirikjian, and G. Fichtinger, "A robust fluoroscope tracking (ftrac) fiducial," *Med Phys* **32**, pp. 3185–98, Oct 2005.
20. Jain et al, "C-arm calibration: is it really necessary?," in *SPIE Medical Imaging 2007, Presented at the Society of Photo-Optical Instrumentation Engineers (SPIE) Conference* **6509**, Mar. 2007.
21. R. Kon, A. Jain, and G. Fichtinger, "Hidden seed reconstruction from c-arm images in brachytherapy," in *IEEE ISBI*, pp. 526–29, Apr 2006.
22. Su et al, "Examination of dosimetry accuracy as a function of seed detection rate in permanent prostate brachytherapy," *Med Phy* **32**, pp. 3049–56, Sep 2005.